POLITECNICO DI TORINO
Repository ISTITUZIONALE

Limitations of Nyquist Criteria in the Discretization of 2D Electromagnetic Integral Equations at High Frequency: Spectral Insights into Pollution Effects

Original
Limitations of Nyquist Criteria in the Discretization of 2D Electromagnetic Integral Equations at High Frequency: Spectral Insights into Pollution Effects / Giunzioni, V., Merlini, A., Andriulli, F.P.. - In: IEEE TRANSACTIONS ON ANTENNAS AND PROPAGATION. - ISSN 0018-926X. - 74:8(2026), pp. 7792-7807. [10.1109/TAP.2026.3694106]

Availability:
This version is available at: 11583/3011530 since: 2026-05-28T16:22:36Z

Publisher:
IEEE

Published
DOI:10.1109/TAP.2026.3694106

Terms of use:

This article is made available under terms and conditions as specified in the corresponding bibliographic description in the repository

Publisher copyright

(Article begins on next page)

26 November 2026

Limitations of Nyquist Criteria in the Discretization of 2-D Electromagnetic Integral Equations at High Frequency: Spectral Insights Into Pollution Effects

Viviana Giunzioni, *Member, IEEE*, Adrien Merlini, *Senior Member, IEEE*, and Francesco P. Andriulli, *Fellow, IEEE*

***Abstract*—Electromagnetic integral equations are typically solved numerically using boundary element methods (BEMs). When the frequency of the wave phenomenon under study increases, the discretization of the problem is typically chosen to maintain a fixed number of unknowns per wavelength. Under these conditions, the BEM over finite-dimensional subspaces of piecewise polynomial basis functions is commonly believed to provide a bounded solution accuracy, at least for nontrapping geometries. If proven, this would constitute a significant advantage of the BEM with respect to finite-element method (FEM) and finite-difference time-domain method, which, in contrast, are affected by numerical dispersion, which causes the number of unknowns per wavelength required to achieve a prescribed solution accuracy to increase with frequency, a phenomenon known as *pollution*. In this work, we conduct a rigorous spectral analysis of some of the most commonly used boundary integral operators and examine the impact of the BEM discretization on the solution accuracy of widely used integral equations modeling the electromagnetic scattering from a perfectly electrically conducting (PEC) cylinder. We consider both ill-conditioned and well-conditioned equations, the latter being characterized by solution operators bounded independently of frequency. Contrary to the common belief, our analysis reveals a form of pollution that affects, in different measures, equations of both kinds. After elucidating the mechanism by which the BEM discretization impacts accuracy, we propose a solution strategy that can cure the pollution problem thus evidenced. The defining strength of the proposed theoretical model lies in its capacity to deliver deep insight into the root causes of the phenomenon.**

***Index Terms*—Aliasing, filtering, hypersingular operator, Nyquist discretization criteria, pollution in the boundary element method (BEM), spectral error.**

I. Introduction

NUMERICAL methods are widely employed to model noncanonical, realistic, scattering problems involving the Helmholtz equation [1], [2]. Finite-element strategies consist in approximating the solution as a linear combination of a finite number of basis functions defined on finite elements.

Received 4 November 2025; revised 23 March 2026; accepted 27 April 2026. Date of publication 22 May 2026; date of current version 6 August 2026. This work has received funding from the European Innovation Council (EIC) through the European Union's Horizon Europe research Programme under Grant 101046748 (Project CEREBRO). *(Corresponding author: Francesco P. Andriulli.)*

Viviana Giunzioni and Francesco P. Andriulli are with the Department of Electronics and Telecommunications, Politecnico di Torino, 10129 Turin, Italy (e-mail: francesco.andriulli@polito.it).

Adrien Merlini is with the Microwave Department, IMT Atlantique, 29238 Brest, France (e-mail: adrien.merlini@imt-atlantique.fr).

Digital Object Identifier 10.1109/TAP.2026.3694106

Let $v_k \in V$ be the oscillatory solution of a boundary value problem governed by the Helmholtz equation of wavenumber k and let V_N be an $N-$dimensional subspace of the Hilbert space V, then the best approximation of v_k in V_N is given by the orthogonal projection [2], [3] $P_N : V \to V_N$ of v_k onto V_N, i.e.,

$$\|(I - P_N)\, v_k\|_V = \min_{w_{k,N} \in V_N} \|v_k - w_{k,N}\|_V . \tag{1}$$

When fixing an error threshold ϵ, we denote by $N_*(\epsilon, k)$ the minimum dimension such that the best approximating function of v_k in the corresponding approximation space $V_{N_*(\epsilon,k)}$ has an error less than or equal to ϵ

$$\left\| \left(I - P_{N_*(\epsilon,k)}\right) v_k \right\|_V \leq \epsilon. \tag{2}$$

To achieve the same accuracy, a numerical method requires a number of unknowns $N_{\text{num}}(\epsilon, k) \geq N_*(\epsilon, k)$. If the ratio $N_{\text{num}}(\epsilon, k)/N_*(\epsilon, k)$ remains bounded as the wavenumber increases, the numerical method is quasi-optimal. In contrast, if the ratio $N_{\text{num}}(\epsilon, k)/N_*(\epsilon, k)$ grows without bound in the high-frequency limit, we say that the numerical method is affected by pollution [4].

From the Weyl law describing the asymptotic behavior of the eigenvalues of the Helmholtz operator [5], [6] or, in the 1-D case, from the Shannon–Nyquist sampling theorem [7], we know that the number of piecewise polynomial basis functions required to accurately approximate a function in $\mathbb{C}^d$ oscillating with frequency $\lesssim k$ is approximately k^d. This means that the natural growth of the number of degrees of freedom is $N \sim k^d$. Rigorous considerations and error bounds can be found in [8] and [9]. Hence, a growth in frequency of the parameter N_{num} higher than k^d denotes pollution.

Some of the most widespread numerical methods, such as the finite-element method (FEM) and the finite-difference method (FDM), are affected by pollution. After the initial observations and analyses of the phenomenon in the 1980s [10], [11], in-depth investigations during the following decade [12], [13], [14] led to a comprehensive understanding of the problem. In particular, the pollution affecting the FEM is related to a phase lag of the numerical solution with respect to the analytic one. In other words, the wavenumber of the numerical solution diverges from the true wavenumber when using a number of finite elements proportional only to k^d, resulting in numerical dispersion. Significant investigations have been directed toward the definition of strategies to minimize the computational burden related to the increase of

© 2026 The Authors. This work is licensed under a Creative Commons Attribution 4.0 License.
For more information, see https://creativecommons.org/licenses/by/4.0/

the ratio $N_{\text{num}}(\epsilon)/N(\epsilon)$ in frequency. While the pollution effect can be avoided in 1-D problems [4], [15], [16], [17], it is not the case in higher dimensional problems [4], [15]. Numerous techniques have been proposed to control and minimize the pollution error in 2-D and 3-D problems. Even though they are capable of significantly mitigating the requirement for bounded accuracy from $hk^2 = \text{const.}$ up to $h^3k^{3.5} = \text{const.}$, where h denotes the size of the elements of the mesh [4], [15], [18], [19], [20], [21], the related numerical dispersion arising at high frequencies represents a significant drawback of finite-element-based simulations.

The boundary element method (BEM) is another popular strategy to numerically solve Helmholtz scattering problems. With respect to FEMs, it only requires the discretization of the boundary of the scatterer and allows for boundary conditions to be enforced automatically, at the cost of building nonsparse linear systems of equations. In the engineering community, it is common practice to numerically solve BEM Helmholtz scattering problems by fixing a number of degrees of freedom per wavelength, that is, by assembling and solving linear systems of size proportional to k^{d-1}, where d is the dimension of the problem [22], [23], [24]. This rule of thumb reflects the common belief that the h-BEM is less affected by numerical pollution than the h-FEM, at least for nontrapping geometries [25], [26]. Various numerical experiments proposed in the literature suggest the quasi-optimality of some boundary integral equations (BIEs) under certain conditions [22], [25]. On the other hand, a form of pollution similar to that observed in the h-FEM has been numerically identified by Marburg [27], [28] in some of his experiments.

Some theoretical investigations resulting in k-explicit quasi-optimality statements about BIEs have been proposed in the numerical analysis literature, mainly focused on the direct and indirect second kind formulations for the exterior Dirichlet problems. Fourier analyses performed on integral operators evaluated over spherical domains [29], [30] have yielded quasi-optimal, frequency-independent, error estimates for the solution of the BEM discretized standard combined equations for the above problem. Similar results for the same equations applied to scatterers bounded by analytic curves or surfaces have been demonstrated in [31]. The analysis proposed is based on a novel decomposition of the combined integral operators [32], which allows for a separate examination of their low- and high-frequency spectral components through Fourier analysis. Based on a similar idea of splitting of diverse frequency components, the work in [26] finally provides a proof of the fact that the Helmholtz exterior Dirichlet problem does not suffer from the pollution effect when the obstacle is nontrapping. The analysis here takes advantage of the concept of semiclassical pseudodifferential operators [33], which, with respect to the standard, or homogeneous, pseudodifferential operators [34], are particularly tailored to the high-frequency analysis required. Further investigations about these topics by some of the same authors are summarized in the preprint [35], expanding the analysis to the Helmholtz exterior Neumann problem solved by means of a Calderón regularization of the standard combined operator, involving the hypersingular operator. However, it is worth noting that, when considering compositions of operators, for simplicity, the authors do not account for the discretization of the operator product in the Galerkin discretization model.

In this work, we propose a fundamentally different approach for analyzing the problem that is based on the spectral Fourier analysis of operator matrices rather than the operators themselves, and is thus capable of explaining the effects of BEM discretization on integral operators and the resulting solution errors. We focus on the 2-D electromagnetic scattering from a perfectly electrically conducting (PEC) circular-cross-sectional cylinder, modeled by electric and magnetic field integral equations (EFIEs/MFIEs), discretized with low-order piecewise polynomials. Within the developed theoretical framework, we derive closed-form expressions for the current and scattering errors resulting from BEM discretization of the formulations under study. Through their high-frequency asymptotic analysis, we identify a form of pollution affecting the transverse electric (TE)-EFIE, which, to the best of the authors' knowledge, has not been previously reported in the literature. Additionally, we extend the analysis to a Calderón-stabilized combined field equation, whose solution operator remains bounded independently of frequency. Our new modeling techniques, because they are capable of tracking and predicting the effects of discretizing a product of operators as a product of matrices that discretize individual operators, reveal negative repercussions of the BEM discretization even on the well-behaved Calderón-stabilized equation. Finally, and most importantly, the proposed analytical approach offers simple yet rigorous explanations of the pollution mechanism, identifying its root causes. This profound understanding of the issue directly opens the way to solution strategies based on operator filtering techniques [36], as demonstrated in this work through both analytical and numerical results.

This article is organized as follows: after setting the background and notation in Section II, we introduce in Section III the spectral error analysis that is the foundation of this work, treating the different operators in various regions of the spectra and compositions of operators. After moving to the current and scattering error analysis in Sections IV and V that show the existence of a pollution effect in some of the equations considered, we delineate in Section VI a filtering strategy capable of suppressing the components of the spectral error increasing in frequency and neutralizing the pollution. Numerical results presented in Section VII validate the theoretical framework. Preliminary and partial results have been previously presented in the conference contribution [37].

II. Background and Notation

Consider the time-harmonic electromagnetic scattering from a PEC circular-cross-sectional cylinder indefinitely extended along the longitudinal direction $\hat{\mathbf{z}}$. Let Ω be the open set modeling the transversal cross section of the cylinder of radius a and $\Gamma := \partial\Omega$ be its circular contour. The exterior space $\mathbb{R}^2\backslash\Omega$ is characterized by its impedance $\eta = \sqrt{\mu/\epsilon}$ and the corresponding wavenumber $k = \omega\sqrt{\mu\epsilon}$. By defining the azimuthal angle $\phi \in [0, 2\pi)$, Γ can be parametrized in ϕ in the 2-D Cartesian plane as $\Gamma = [a\cos(\phi), a\sin(\phi)]^{\mathrm{T}}$.

The single-layer, double-layer, adjoint double-layer, and hypersingular operators are defined as

$$\mathcal{S}^k f(\boldsymbol{\rho}) := k \int_\Gamma G^k(\boldsymbol{\rho},\boldsymbol{\rho}') f(\boldsymbol{\rho}') \, d\boldsymbol{\rho}' \tag{3}$$

$$\mathcal{D}^k f(\boldsymbol{\rho}) := \int_\Gamma \frac{\partial}{\partial n'} G^k(\boldsymbol{\rho},\boldsymbol{\rho}') f(\boldsymbol{\rho}') \, d\boldsymbol{\rho}' \tag{4}$$

$$\mathcal{D}^{*k} f(\boldsymbol{\rho}) := \int_\Gamma \frac{\partial}{\partial n} G^k(\boldsymbol{\rho},\boldsymbol{\rho}') f(\boldsymbol{\rho}') \, d\boldsymbol{\rho}' \tag{5}$$

$$\mathcal{N}^k f(\boldsymbol{\rho}) := -\frac{1}{k}\frac{\partial}{\partial n} \int_\Gamma \frac{\partial}{\partial n'} G^k(\boldsymbol{\rho},\boldsymbol{\rho}') f(\boldsymbol{\rho}') \, d\boldsymbol{\rho}'. \tag{6}$$

The 2-D free-space Green's function is $G^k(\boldsymbol{\rho},\boldsymbol{\rho}') := -\mathrm{j}/4 H_0^{(2)}(k|\boldsymbol{\rho} - \boldsymbol{\rho}'|)$, where $H_0^{(2)}$ is the Hankel function of the second kind [38]. These are the building blocks for the EFIE and MFIE, which relate the longitudinal and transversal electric current densities J_z and J_t to the impinging electromagnetic fields (E_z, H_t) and (E_t, H_z) [39], [40], [41]. In the transverse magnetic (TM) polarization, they read

$$\mathcal{S}^k(J_z)(\boldsymbol{\rho}) = \frac{E_z(\boldsymbol{\rho})}{\mathrm{j}\eta} \tag{7}$$

$$\left(\frac{1}{2}\mathcal{I} + \mathcal{D}^{*k}\right)(J_z)(\boldsymbol{\rho}) = H_t(\boldsymbol{\rho}) \tag{8}$$

while in the TE polarization, they read

$$\mathcal{N}^k(J_t)(\boldsymbol{\rho}) = -\frac{E_t(\boldsymbol{\rho})}{\mathrm{j}\eta} \tag{9}$$

$$\left(\frac{1}{2}\mathcal{I} - \mathcal{D}^{k}\right)(J_t)(\boldsymbol{\rho}) = -H_z(\boldsymbol{\rho}). \tag{10}$$

In this work, we will study the regime in which the number of degrees of freedom used in the discretization of the problem increases proportionally with the frequency, which is equivalent to fixing a constant number of unknowns per wavelength; this setting is often referred to as the high-frequency regime [42].

In this regime, the EFIE and MFIE suffer from several sources of instability such as spurious resonances, manifesting themselves as a finite number of eigenvalues of the operators going to zero [42], [43], or the high-frequency breakdown, which is a growth of the condition number as the frequency increases. In particular, the condition number of the matrices discretizing the TM- and TE-EFIE grows in frequency as $\mathcal{O}((ka)^{1/3})$ as $ka \to \infty$ away from resonances [44], [45]. Both issues can be addressed, for a class of scatterers, by combining and preconditioning the EFIE and MFIE to form the Calderón combined field integral equation (CCFIE) [46], [47], denoted in the following as "CCFIE," that reads for TM and TE polarizations, respectively:

$$\begin{aligned}&\left[\mathcal{N}^{\tilde{k}}\mathcal{S}^k + \left(\frac{1}{2}\mathcal{I} - \mathcal{D}^{*\tilde{k}}\right)\left(\frac{1}{2}\mathcal{I} + \mathcal{D}^{*k}\right)\right](J_z)(\boldsymbol{\rho}) \\ &= \frac{\mathcal{N}^{\tilde{k}}}{\mathrm{j}\eta} E_z(\boldsymbol{\rho}) + \left(\frac{1}{2}\mathcal{I} - \mathcal{D}^{*\tilde{k}}\right) H_t(\boldsymbol{\rho})\end{aligned} \tag{11}$$

$$\begin{aligned}&\left[\mathcal{S}^{\tilde{k}}\mathcal{N}^k + \left(\frac{1}{2}\mathcal{I} + \mathcal{D}^{\tilde{k}}\right)\left(\frac{1}{2}\mathcal{I} - \mathcal{D}^{k}\right)\right](J_t)(\boldsymbol{\rho}) \\ &= -\frac{\mathcal{S}^{\tilde{k}}}{\mathrm{j}\eta} E_t(\boldsymbol{\rho}) - \left(\frac{1}{2}\mathcal{I} + \mathcal{D}^{\tilde{k}}\right) H_z(\boldsymbol{\rho})\end{aligned} \tag{12}$$

where $\tilde{k} := k - \mathrm{j}0.4k^{1/3}a^{-2/3}$. The interested reader can refer to several excellent works in the literature [48], [49], [50] for more details on this particular choice of complex wavenumber. The complex wavenumber employed in the evaluation of the preconditioning operator matrices is shown to be optimal over the circle of radius a, and its use allows one to define Calderón combined field integral operators (CCFIOs), which are bounded and whose inverses are bounded in the high-frequency limit [46], [47].

To discretize and numerically solve the above integral equations, we consider a uniform discretization of the boundary Γ composed of N circular arcs of length $h = 2\pi a/N$. The vertices of these elements lie at the points $[a\cos(\phi_n), a\sin(\phi_n)]^{\mathrm{T}}$, where $\phi_n := 2\pi n/N$ for $n = 0, \ldots, N-1$. In the following, we will assume N odd for simplicity and without loss of generality. We further introduce the parameter $n_\lambda := \lfloor 2\pi/(kh) \rfloor$, quantifying the ratio between the wavelength and the mesh parameter h.

Over this mesh, we define a set of N pyramidal, or Lagrangian, basis functions $\{f_i\}_{i=0}^{N-1}$ attached over the N vertices and having domain $2h$. In particular, f_0 is defined as

$$f_0(r) = \begin{cases} \dfrac{1}{h}(a\phi_1 - r), & \text{if } 0 \le r < a\phi_1 \\ \dfrac{1}{h}(r - a\phi_{N-1}), & \text{if } a\phi_{N-1} \le r < a\left(\phi_{N-1} + \frac{2\pi}{N}\right) \end{cases}$$

and f_i is given by $f_i(r) = f_0(r - a\phi_i)$, where we have denoted by $r := a\phi$ the curvilinear abscissa. By following the standard Galerkin procedure, we expand the unknowns of the above integral equations as linear combinations of the basis functions $\{f_i\}_{i=0}^{N-1}$ and test the resulting equations with test functions of the same kind, resulting in the linear systems:

$$\boldsymbol{S}^k \hat{\boldsymbol{J}}_z = \boldsymbol{E}_z/(\mathrm{j}\eta) \tag{13}$$

$$\left(\boldsymbol{G}/2 + \boldsymbol{D}^{*k}\right)\hat{\boldsymbol{J}}_z = \boldsymbol{H}_t \tag{14}$$

$$\boldsymbol{N}^k \hat{\boldsymbol{J}}_t = -\boldsymbol{E}_t/(\mathrm{j}\eta) \tag{15}$$

$$\left(\boldsymbol{G}/2 - \boldsymbol{D}^{k}\right)\hat{\boldsymbol{J}}_t = -\boldsymbol{H}_z \tag{16}$$

$$\begin{aligned}\boldsymbol{C}^{\mathrm{TM}}\hat{\boldsymbol{J}}_z &:= \left[\boldsymbol{N}^{\tilde{k}}\boldsymbol{G}^{-1}\boldsymbol{S}^k + \left(\boldsymbol{G}/2 - \boldsymbol{D}^{*\tilde{k}}\right)\right. \\ &\qquad \left.\boldsymbol{G}^{-1}\left(\boldsymbol{G}/2 + \boldsymbol{D}^{*k}\right)\right]\hat{\boldsymbol{J}}_z \\ &= \boldsymbol{N}^{\tilde{k}}\boldsymbol{G}^{-1}\boldsymbol{E}_z/(\mathrm{j}\eta) + \left(\boldsymbol{G}/2 - \boldsymbol{D}^{*\tilde{k}}\right)\boldsymbol{G}^{-1}\boldsymbol{H}_t\end{aligned} \tag{17}$$

$$\begin{aligned}\boldsymbol{C}^{\mathrm{TE}}\hat{\boldsymbol{J}}_t &:= \left[\boldsymbol{S}^{\tilde{k}}\boldsymbol{G}^{-1}\boldsymbol{N}^k + \left(\boldsymbol{G}/2 + \boldsymbol{D}^{\tilde{k}}\right)\right. \\ &\qquad \left.\boldsymbol{G}^{-1}\left(\boldsymbol{G}/2 - \boldsymbol{D}^{k}\right)\right]\hat{\boldsymbol{J}}_t \\ &= -\boldsymbol{S}^{\tilde{k}}\boldsymbol{G}^{-1}\boldsymbol{E}_t/(\mathrm{j}\eta) - \left(\boldsymbol{G}/2 + \boldsymbol{D}^{\tilde{k}}\right)\boldsymbol{G}^{-1}\boldsymbol{H}_z\end{aligned} \tag{18}$$

where the element (m,n) of a matrix $\boldsymbol{O}$, which acts as a placeholder for $\boldsymbol{S}$, $\boldsymbol{N}$, $\boldsymbol{D}$, $\boldsymbol{D}^*$, and $\boldsymbol{G}$, is

$$\boldsymbol{O}_{mn} = \frac{1}{h}\int_0^{2\pi a} \mathrm{d}r\, f_m(r)\ (\mathcal{O} f_n(r)) \tag{19}$$

where $\mathcal{O}$ stands for $\mathcal{S}$, $\mathcal{N}$, $\mathcal{D}$, $\mathcal{D}^*$, and $\mathcal{I}$ (where $\mathcal{I}$ denotes the identity operator), and the nth element of the array $\boldsymbol{F}$, where $\boldsymbol{F}$ stands for $\boldsymbol{E}_z$, $\boldsymbol{H}_t$, $\boldsymbol{E}_t$, and $\boldsymbol{H}_z$, is given by

$$\boldsymbol{F}_n = \frac{1}{h}\int_0^{2\pi a} \mathrm{d}r\, f_n(r) F(r) \tag{20}$$

where F stands for E_z, H_t, E_t, and H_z. The arrays $\hat{\boldsymbol{J}}_z$ and $\hat{\boldsymbol{J}}_t$ contain the weights of the linear combinations of pyramid basis functions expanding the unknown functions.

Because Γ is a circle, one can derive closed-form expressions for the qth eigenvalue $\lambda_q^{\mathcal{O}}$ of a continuous operator $\mathcal{O}$ [51], [52], which for the operators under study yields

$$\lambda_q^{\mathcal{S}^k} = -\frac{\mathrm{j}k\pi a}{2} J_q(ka)\, H_q^{(2)}(ka) \tag{21}$$

$$\lambda_q^{\mathcal{D}^k} = \lambda_q^{\mathcal{D}^{*k}} = -\frac{\mathrm{j}k\pi a}{4}\left[J_q(ka)\, H_q^{(2)}(ka)\right]' \tag{22}$$

$$\lambda_q^{\mathcal{N}^k} = \frac{\mathrm{j}k\pi a}{2} J_q'(ka)\, H_q^{(2)\prime}(ka) \tag{23}$$

where $J_q(ka)$ and $H_q^{(2)}(ka)$ denote the Bessel function of the first kind and the Hankel function of the second kind of order q and argument (ka). Note that these functions are linked by the equality $H_q^{(2)}(ka) = J_q(ka) - \mathrm{j}Y_q(ka)$, where Y_q is the Bessel function of second kind and order q [38]. On the circular domain Γ, these operators share the same eigenfunctions and thus commute with one another. In particular, the eigenfunction associated with the eigenvalue $\lambda_q^{\mathcal{O}}$ is the complex exponential $\phi \mapsto \mathrm{e}^{-\mathrm{j}q\phi}$ [51]. From this commutative property, we can infer that the eigenvalues of the TM/TE-magnetic field integral operator (MFIO), $\mathcal{I}/2 + \mathcal{D}^{*k}$ and $\mathcal{I}/2 - \mathcal{D}^k$, are [38], [53]

$$\lambda_q^{\text{TM-MFIO}^k} = -\frac{\mathrm{j}\pi ka}{2} J_q'(ka)\, H_q^{(2)}(ka) \tag{24}$$

$$\lambda_q^{\text{TE-MFIO}^k} = \frac{\mathrm{j}\pi ka}{2} J_q(ka)\, H_q^{(2)\prime}(ka)\,. \tag{25}$$

On the particular geometrical and functional setting described above, the eigenvalues of the operator matrices are also known in closed form [54], [55], [56] and can be expressed as

$$\hat{\lambda}_q^{\boldsymbol{O}} = \sum_{s=-\infty}^{\infty} \lambda_{(q+sN)}^{\mathcal{O}} F_{-(q+sN)} F_{(q+sN)} \tag{26}$$

where F_q represents the qth Fourier coefficient of the function f_0 [44], [56]

$$F_q := \frac{N}{2\pi}\int \mathrm{d}\phi f_0(\phi)\, e^{\mathrm{j}q\phi} = \left(\frac{\sin(\pi q/N)}{(\pi q/N)}\right)^2. \tag{27}$$

Equation (26) is exact if the matrices are obtained in infinite precision and infinite accuracy. Following from the application of the Green's function addition theorem, the analysis leading to the definition of $\hat{\lambda}_q^{\boldsymbol{O}}$ also shows that the eigenvectors of the matrices are shared between different operator matrices and simply correspond to the discretization of the continuous eigenfunctions, $\phi \mapsto e^{-\mathrm{j}q\phi}$, in the chosen functional basis.

The spectral relative difference between continuous and discrete eigenvalues can be derived from the knowledge of both $\lambda_q^{\boldsymbol{O}}$ and $\hat{\lambda}_q^{\boldsymbol{O}}$ as

$$E_q^{\mathcal{O}} := \frac{\hat{\lambda}_q^{\boldsymbol{O}} - \lambda_q^{\mathcal{O}}}{\lambda_q^{\mathcal{O}}} = E_q^P + E_q^{A,\mathcal{O}} \tag{28}$$

where

$$E_q^P := F_{-q}F_q - 1 \tag{29}$$

$$E_q^{A,\mathcal{O}} := \frac{1}{\lambda_q^{\mathcal{O}}}\sum_{s\neq 0} \lambda_{(q+sN)}^{\mathcal{O}} F_{-(q+sN)} F_{(q+sN)} \tag{30}$$

represent the spectral projection and aliasing error contributions, respectively [44], [56].

III. Spectral Error Analysis

We aim at analyzing the spectral relative error (28) in the high-frequency regime. The analysis will also include the spectral error of the combinations and products of integral operators, such as the ones appearing in the MFIO and in the CCFIO.

A. Sums and Products of Operators

Given two matrices $\boldsymbol{M}$ and $\boldsymbol{N}$ that share the same eigenvectors and with eigenvalues $\hat{\lambda}_q^{\mathcal{M}} = \lambda_q^{\mathcal{M}}(1 + E_q^{\mathcal{M}})$ and $\hat{\lambda}_q^{\mathcal{N}} = \lambda_q^{\mathcal{N}}(1 + E_q^{\mathcal{N}})$ [with $E_q^{\mathcal{M}}$ and $E_q^{\mathcal{N}}$ in the form of (28)], the qth eigenvalue of their sum $(\boldsymbol{M} + \boldsymbol{N})$ is $(\hat{\lambda}_q^{\mathcal{M}} + \hat{\lambda}_q^{\mathcal{N}})$, with relative error with respect to $(\lambda_q^{\mathcal{M}} + \lambda_q^{\mathcal{N}})$ given by

$$\begin{aligned} E_q^{\mathcal{M}+\mathcal{N}} &= \frac{\left(\hat{\lambda}_q^{\mathcal{M}} + \hat{\lambda}_q^{\mathcal{N}}\right) - \left(\lambda_q^{\mathcal{M}} + \lambda_q^{\mathcal{N}}\right)}{\left(\lambda_q^{\mathcal{M}} + \lambda_q^{\mathcal{N}}\right)} \\ &= E_q^P + \frac{\lambda_q^{\mathcal{M}} E_q^{A,\mathcal{M}} + \lambda_q^{\mathcal{N}} E_q^{A,\mathcal{N}}}{\lambda_q^{\mathcal{M}} + \lambda_q^{\mathcal{N}}} \end{aligned} \tag{31}$$

in which the second term represents the aliasing error of the sum of the two operators. The qth eigenvalue of their product $(\boldsymbol{MN})$ is $\hat{\lambda}_q^{\mathcal{M}}\hat{\lambda}_q^{\mathcal{N}}$, with its relative error with respect to $\lambda_q^{\mathcal{M}}\lambda_q^{\mathcal{N}}$ given by

$$\begin{aligned} E_q^{\mathcal{M}\cdot\mathcal{N}} &= \frac{\left(\hat{\lambda}_q^{\mathcal{M}}\hat{\lambda}_q^{\mathcal{N}}\right) - \left(\lambda_q^{\mathcal{M}}\lambda_q^{\mathcal{N}}\right)}{\left(\lambda_q^{\mathcal{M}}\lambda_q^{\mathcal{N}}\right)} \\ &= E_q^{\mathcal{M}} + E_q^{\mathcal{N}} + E_q^{\mathcal{M}} E_q^{\mathcal{N}}. \end{aligned} \tag{32}$$

B. Spectral Aliasing Error

Different from the projection error (29), which only depends on the discretization through the coefficient F_q, the aliasing error (30) is strictly associated with the continuous operator from which the matrix derives. Hence, to understand the high-frequency behavior of the aliasing spectral error of the formulations under test, we need to study the behavior of the eigenvalues of the integral operators in the high-frequency limit. The analysis will be performed in three spectral regions: the hyperbolic region of propagative modes at indices $q \ll ka$, the transition region of modes at indices $q \simeq ka$, and the elliptic region of evanescent modes at indices $q \gg ka$ [57].

1) Eigenvalues in the Hyperbolic Region: To study the behavior of the eigenvalues of the operators in the hyperbolic region [29], we use the large-argument principal asymptotic expansions of the Bessel and Hankel functions [38, Eq. 9.2.1, 9.2.4] valid for fixed positive indices and growing argument. It follows that the operator eigenvalues in the hyperbolic region in the high-frequency limit can be approximated as:

$$\lambda_q^{\mathcal{S}^k} \sim -\mathrm{j}e^{-\mathrm{j}\beta}\cos(\beta) \tag{33}$$

$$\lambda_q^{\mathcal{N}^k} \sim -\sqrt{\mathrm{j}}e^{-\mathrm{j}\gamma}\sin(\beta) \tag{34}$$

$$\lambda_q^{\text{TM-MFIO}^k} \sim \mathrm{j}\sqrt{\mathrm{j}}e^{-\mathrm{j}\gamma}\sin(\beta) \tag{35}$$

$$\lambda_q^{\text{TE-MFIO}^k} \sim e^{-\mathrm{j}\beta}\cos(\beta) \tag{36}$$

$$\lambda_q^{\mathcal{D}^k} \sim -\mathrm{j}e^{-2\mathrm{j}\gamma}/2 \tag{37}$$

where $\beta = ka - q\pi/2 - \pi/4$, $\gamma = \beta + \pi/4$, and the symbol $\sim$ indicates an asymptotic equality [38]. These expressions show that $\lambda_q^{\mathcal{S}^k}$ and $\lambda_q^{\mathcal{N}^k}$ have a constant behavior in frequency away from resonances, both in real and imaginary parts. The same holds true for the eigenvalues of the MFIO and of the double-layer operator.

2) Eigenvalues in the Transition Region: To study the behavior of the eigenvalues of the operators in the transition region [29], [44], we leverage the large-order asymptotic expansions of the Bessel and Hankel functions and of their derivatives in the transition region. The asymptotic expansions [38, eqs. 9.3.31–.3.34] read

$$J_q(q) \sim q^{-1/3}\mu\Sigma_\alpha - q^{-5/3}\nu\Sigma_\beta \tag{38}$$

$$Y_q(q) \sim -q^{-1/3}\sqrt{3}\mu\Sigma_\alpha - q^{-5/3}\sqrt{3}\nu\Sigma_\beta \tag{39}$$

$$J_q'(q) \sim q^{-2/3}\nu\Sigma_\gamma - q^{-4/3}\mu\Sigma_\delta \tag{40}$$

$$Y_q'(q) \sim q^{-2/3}\sqrt{3}\nu\Sigma_\gamma + q^{-4/3}\sqrt{3}\mu\Sigma_\delta \tag{41}$$

where μ, ν, Σ_α, Σ_β, Σ_γ, and Σ_δ are real quantities. As a consequence, the operator eigenvalues in the transition region can be approximated as

$$\lambda_q^{\mathcal{S}^k} \sim \frac{\pi}{2}q^{-7/3}\left(\mu\Sigma_\alpha q^{4/3} - \nu\Sigma_\beta\right)\left(\left(\sqrt{3}+\mathrm{j}\right)\nu\Sigma_\beta + \left(\sqrt{3}-\mathrm{j}\right)\mu\Sigma_\alpha q^{4/3}\right) \tag{42}$$

$$\lambda_q^{\mathcal{N}^k} \sim \frac{\pi}{2}q^{-5/3}\left(\nu\Sigma_\gamma q^{2/3} - \mu\Sigma_\delta\right)\left(\left(\sqrt{3}-\mathrm{j}\right)\mu\Sigma_\delta + \left(\sqrt{3}+\mathrm{j}\right)\nu\Sigma_\gamma q^{2/3}\right) \tag{43}$$

$$\lambda_q^{\text{TM-MFIO}^k} \sim \frac{\pi}{2}q^{-2}\left(\nu\Sigma_\gamma q^{2/3} - \mu\Sigma_\delta\right)\left(\left(\sqrt{3}+\mathrm{j}\right)\nu\Sigma_\beta + \left(\sqrt{3}-\mathrm{j}\right)\mu\Sigma_\alpha q^{4/3}\right) \tag{44}$$

$$\lambda_q^{\text{TE-MFIO}^k} \sim \frac{\pi}{2}q^{-2}\left(\mu\Sigma_\alpha q^{4/3} - \nu\Sigma_\beta\right)\left(\left(\sqrt{3}-\mathrm{j}\right)\mu\Sigma_\delta + \left(\sqrt{3}+\mathrm{j}\right)\nu\Sigma_\gamma q^{2/3}\right) \tag{45}$$

$$\lambda_q^{\mathcal{D}^k} \sim \frac{\pi}{2}q^{-2}\left(-\mathrm{j}\mu\nu\left(q^2\Sigma_\alpha\Sigma_\gamma + \Sigma_\beta\Sigma_\delta\right) + \left(\sqrt{3}+\mathrm{j}\right)\nu^2\Sigma_\beta\Sigma_\gamma q^{2/3} - \left(\sqrt{3}-\mathrm{j}\right)\mu^2\Sigma_\alpha\Sigma_\delta q^{4/3}\right). \tag{46}$$

These expressions show that, in the transition region, the eigenvalues of the single-layer operator behave as $q^{1/3} \simeq (ka)^{1/3}$ in both real and imaginary parts, while the eigenvalues of the hypersingular operator behave as $q^{-1/3} \simeq (ka)^{-1/3}$ in both real and imaginary parts. In addition, the eigenvalues of the MFIO are bounded in the high-frequency limit in real and imaginary parts, consistently with the constant behavior of the imaginary part of $\lambda_q^{\mathcal{D}^k}$ and with the decrease of the real part of $\lambda_q^{\mathcal{D}^k}$, decaying in frequency as $q^{-2/3} \simeq (ka)^{-2/3}$.

3) Eigenvalues in the Elliptic Region: The behavior of the eigenvalues of the operators in the elliptic region [29], [44] can be studied by resorting to the large-order asymptotic expansions of the Bessel and Hankel functions [58, eqs. 10.19.1 and 10.19.2] and of their derivatives with respect to the argument

$$J_\nu'(z) \sim \sqrt{\frac{\nu}{2\pi}}\left(\frac{ez}{2\nu}\right)^\nu\frac{1}{z} \tag{47}$$

$$H_\nu^{(2)'}(z) \sim -\mathrm{j}\sqrt{\frac{2}{\nu\pi}}\left(\frac{ez}{2\nu}\right)^{-\nu}\frac{\nu}{z} \tag{48}$$

from which we obtain

$$\lambda_q^{\mathcal{S}^k} \sim \frac{ka}{2q} \tag{49}$$

$$\lambda_q^{\mathcal{N}^k} \sim \frac{q}{2ka} \tag{50}$$

$$\lambda_q^{\text{TM-MFIO}^k} \sim \frac{1}{2} \tag{51}$$

$$\lambda_q^{\text{TE-MFIO}^k} \sim \frac{1}{2}. \tag{52}$$

Moreover, by expanding the derivatives of the Bessel and Hankel functions as in [58, eq.10.6.1] and employing [58.19.1 and 10.19.2], we obtain

$$\lambda_q^{\mathcal{D}^k} \sim \frac{1}{16\mathrm{e}}\left[4\left(\left(\frac{q-1}{q}\right)^{\frac{1}{2}-q} - \left(\frac{q+1}{q}\right)^{\frac{1}{2}+q}\right) + \mathrm{e}^2(ka)^2\left(\frac{q^{-\frac{1}{2}-q}}{(q-1)^{\frac{3}{2}-q}} - \frac{q^{-\frac{1}{2}+q}}{(q+1)^{\frac{3}{2}+q}}\right)\right]. \tag{53}$$

These expansions show a decay of the eigenvalues $\lambda_q^{\mathcal{S}^k}$ and $\lambda_q^{\mathcal{D}^k}$ in the elliptic region of the spectrum, respectively, as q^{-1} and q^{-3}, while the eigenvalues $\lambda_q^{\mathcal{N}^k}$ increase instead as q. Finally, we are interested in the behavior of eigenvalues at spectral indices $|q| \simeq \kappa ka$, with $\kappa > 1$ fixed, for example, at $|q| \simeq n_\lambda ka/2$ at the edge of the visible discrete bandwidth. From the equations above, it follows that it is constant in the single-layer and hypersingular operator cases, while it decreases as $(ka)^{-1}$ in the double-layer operator case.

C. Aliasing Error of Operators

From the information about the high-frequency behavior of the eigenvalues of the operators in the three different regions, we can infer the high-frequency behavior of the aliasing spectral error of operators.

By comparing the single-layer and hypersingular operators, an asymmetry between them appears clearly: their eigenvalues at spectral indices $|q| \simeq \kappa ka$, with $\kappa > 1$ fixed, in the elliptic region are approximately constant in frequency, while they increase and decrease in modulus, respectively, as $(ka)^{1/3}$ and $(ka)^{-1/3}$ in the transition region. Hence, given the proportionality of N with (ka), the summation term in (30) is approximately constant in frequency. It follows that the aliasing spectral error, respectively, decreases as $(ka)^{-1/3}$ and increases as $(ka)^{1/3}$ in the transition region for the single-layer and hypersingular operators; this behavior is determined by the inverse of the corresponding eigenvalues in the transition region. In the case of the single-layer operator, the spectral aliasing error is often negligible with respect to the

projection error, which asymptotically dictates a bounded-in-frequency relative spectral difference between the continuous and discrete single-layer operator (28) in the transition region. In the case of the hypersingular operator, instead, either the projection or the aliasing error in the summation (28) can be dominant in the transition region depending on the discretization parameter n_λ and on the value of ka. In particular, given the increase in frequency of one spectral error component, while the other stays bounded, for a fixed discretization n_λ, one may always identify the threshold frequency $(ka)_{\text{th}}$ above which the aliasing error $|E^{A,\mathcal{N}^k}_{(ka)}|$ is dominant with respect to the projection error $|E^{P}_{(ka)}|$. Overall, the aliasing spectral error of the hypersingular operator determines an asymptotic increase of the relative spectral difference between the operator and its discrete counterpart in the transition region as $(ka)^{1/3}$ in the high-frequency regime.

Regarding the double-layer operator, given the constant behavior of the modulus of the eigenvalues in the transition region and the decay as $(ka)^{-1}$ at the bandwidth edge, the spectral aliasing error $|E^{A,\mathcal{D}^k}_q|$ decreases as $(ka)^{-1}$ in the transition region. Moreover, as the imaginary part of the eigenvalues of $\mathcal{D}$ is dominant in the transition region, $E^{A,\mathcal{D}^k}_q$ is characterized by a different high-frequency behavior in the real and imaginary components, that is, $|\Re(E^{A,\mathcal{D}^k}_q)|$ behaves as $(ka)^{-5/3}$ and $|\Im(E^{A,\mathcal{D}^k}_q)|$ behaves as $(ka)^{-1}$.

To summarize, in the transition region in the high-frequency limit

$$\left|\Re\left(E^{A,\mathcal{S}^k}_q\right)\right| = \mathcal{O}\left((ka)^{-1/3}\right), \left|\Im\left(E^{A,\mathcal{S}^k}_q\right)\right| = \mathcal{O}\left((ka)^{-1/3}\right), \tag{54}$$

$$\left|\Re\left(E^{A,\mathcal{N}^k}_q\right)\right| = \mathcal{O}\left((ka)^{1/3}\right) \ , \left|\Im\left(E^{A,\mathcal{N}^k}_q\right)\right| = \mathcal{O}\left((ka)^{1/3}\right), \tag{55}$$

$$\left|\Re\left(E^{A,\mathcal{D}^k}_q\right)\right| = \mathcal{O}\left((ka)^{-5/3}\right), \left|\Im\left(E^{A,\mathcal{D}^k}_q\right)\right| = \mathcal{O}\left((ka)^{-1}\right). \tag{56}$$

D. Aliasing Error of the MFIO

Using (31), the spectral relative difference between the continuous MFIO and its discretization can be written

$$\begin{aligned} E^{\text{TM-MFIO}}_q &= \frac{\hat{\lambda}^{\text{TM-MFIO}}_q - \lambda^{\text{TM-MFIO}}_q}{\lambda^{\text{TM-MFIO}}_q} \\ &= E^P_q + \frac{\frac{1}{2}E^{A,\mathcal{I}}_q + \lambda^{\mathcal{D}^*}_q E^{A,\mathcal{D}^*}_q}{\frac{1}{2} + \lambda^{\mathcal{D}^*}_q} \end{aligned} \tag{57}$$

$$\begin{aligned} E^{\text{TE-MFIO}}_q &= \frac{\hat{\lambda}^{\text{TE-MFIO}}_q - \lambda^{\text{TE-MFIO}}_q}{\lambda^{\text{TE-MFIO}}_q} \\ &= E^P_q + \frac{\frac{1}{2}E^{A,\mathcal{I}}_q - \lambda^{\mathcal{D}}_q E^{A,\mathcal{D}}_q}{\frac{1}{2} - \lambda^{\mathcal{D}}_q}. \end{aligned} \tag{58}$$

Hence, the spectral error is composed of two parts, which are a projection component E^P_q, irrespective of the operators under test, and an aliasing component, given by the weighted arithmetic average between the aliasing spectral errors of the operators summed.

As evidenced by (56), the aliasing error contribution $|E^{A,\mathcal{D}}_q|$ in the transition region decays as the inverse of the frequency. However, in the high-frequency limit, this is shadowed by the aliasing contribution from the identity operator, which results in a bounded-in-frequency aliasing (and overall) spectral error of the MFIO. Overall, in the transition region in the high-frequency limit

$$\left|\Re\left(E^{A,\text{TM/TE-MFIO}^k}_q\right)\right| = \mathcal{O}(1) \ , \quad \left|\Im\left(E^{A,\text{TM/TE-MFIO}^k}_q\right)\right| = \mathcal{O}(1). \tag{59}$$

E. Aliasing Error of the CCFIO

The qth eigenvalue of a sum of products of commuting operators is given by the same sum of products of the qth eigenvalues of these operators. Hence, the qth eigenvalue of the CCFIO is given by

$$\begin{aligned} \lambda^{\text{TM-CCFIO}}_q &= \lambda^{\mathcal{N}^{\tilde{k}}}_q \lambda^{\mathcal{S}^k}_q + \lambda^{\text{TE-MFIO}^{\tilde{k}}}_q \lambda^{\text{TM-MFIO}^k}_q \\ &=: \lambda^{\text{TM-CEFIE}}_q + \lambda^{\text{TM-CMFIE}}_q \end{aligned} \tag{60}$$

$$\begin{aligned} \lambda^{\text{TE-CCFIO}}_q &= \lambda^{\mathcal{S}^{\tilde{k}}}_q \lambda^{\mathcal{N}^k}_q + \lambda^{\text{TM-MFIO}^{\tilde{k}}}_q \lambda^{\text{TE-MFIO}^k}_q \\ &=: \lambda^{\text{TE-CEFIE}}_q + \lambda^{\text{TE-CMFIE}}_q. \end{aligned} \tag{61}$$

We next need to estimate the relative spectral difference between the eigenvalues of the continuous operators and the ones of the discretizing matrices resulting from the matrix products and sums in the definitions of $\boldsymbol{C}^{\text{TM}}$ (17) and $\boldsymbol{C}^{\text{TE}}$ (18). Since all the contributions in the TM- and TE-CCFIO are commuting, their eigenvalues are, respectively, given by

$$\hat{\lambda}^{\text{TM-CCFIO}}_q = \frac{\hat{\lambda}^{\mathcal{N}^{\tilde{k}}}_q \hat{\lambda}^{\mathcal{S}^k}_q}{\hat{\lambda}^{\mathcal{I}}_q} + \frac{\left(\hat{\lambda}^{\mathcal{I}}_q/2 - \hat{\lambda}^{\mathcal{D}^{*\tilde{k}}}_q\right)\left(\hat{\lambda}^{\mathcal{I}}_q/2 + \hat{\lambda}^{\mathcal{D}^{*k}}_q\right)}{\hat{\lambda}^{\mathcal{I}}_q} \tag{62}$$

$$\hat{\lambda}^{\text{TE-CCFIO}}_q = \frac{\hat{\lambda}^{\mathcal{S}^{\tilde{k}}}_q \hat{\lambda}^{\mathcal{N}^k}_q}{\hat{\lambda}^{\mathcal{I}}_q} + \frac{\left(\hat{\lambda}^{\mathcal{I}}_q/2 + \hat{\lambda}^{\mathcal{D}^{\tilde{k}}}_q\right)\left(\hat{\lambda}^{\mathcal{I}}_q/2 - \hat{\lambda}^{\mathcal{D}^k}_q\right)}{\hat{\lambda}^{\mathcal{I}}_q}. \tag{63}$$

Using (32), the relative spectral difference is given by the weighted mean

$$E^{\text{TX-CCFIO}}_q = \frac{\lambda^{\text{TX-CEFIO}}_q E^{\text{TX-CEFIO}}_q + \lambda^{\text{TX-CMFIO}}_q E^{\text{TX-CMFIO}}_q}{\lambda^{\text{TX-CEFIO}}_q + \lambda^{\text{TX-CMFIO}}_q} \tag{64}$$

where TX denotes either TM or TE, and the error contributions are

$$E^{\text{TM-CEFIO}}_q = \frac{\left(1 + E^{\mathcal{N}^{\tilde{k}}}_q\right)\left(1 + E^{\mathcal{S}^k}_q\right)}{\left(1 + E^{\mathcal{I}}_q\right)} - 1 \tag{65}$$

$$E^{\text{TM-CMFIO}}_q = \frac{\left(1 + E^{\text{TE-MFIO}^{\tilde{k}}}_q\right)\left(1 + E^{\text{TM-MFIO}^k}_q\right)}{\left(1 + E^{\mathcal{I}}_q\right)} - 1 \tag{66}$$

$$E^{\text{TE-CEFIO}}_q = \frac{\left(1 + E^{\mathcal{S}^{\tilde{k}}}_q\right)\left(1 + E^{\mathcal{N}^k}_q\right)}{\left(1 + E^{\mathcal{I}}_q\right)} - 1 \tag{67}$$

$$E^{\text{TE-CMFIO}}_q = \frac{\left(1 + E^{\text{TM-MFIO}^{\tilde{k}}}_q\right)\left(1 + E^{\text{TE-MFIO}^k}_q\right)}{\left(1 + E^{\mathcal{I}}_q\right)} - 1. \tag{68}$$

The weights $\lambda^{\text{TX-CEFIO}}_q$ and $\lambda^{\text{TX-CMFIO}}_q$ are of similar importance away from resonances. As the spectral error $|E^{\text{TX-MFIO}}_q|$ has a constant behavior in the high-frequency regime, the error contributions $|E^{\text{TM-CMFIO}}_q|$ and $|E^{\text{TE-CMFIO}}_q|$ will also be characterized by a constant behavior. Differently, $|E^{\text{TM-CEFIO}}_q|$

and $|E_q^{\text{TE-CEFIO}}|$ will be negatively affected by the increase of $|E_q^{\mathcal{N}}|$. In conclusion, this will result in an asymptotically increasing behavior of $|E_q^{\text{TM-CCFIO}}|$ and $|E_q^{\text{TE-CCFIO}}|$ as $(ka)^{1/3}$ in the transition region

$$\left|\Re\left(E_q^{A,\text{TM-CCFIO}}\right)\right| = \mathcal{O}\left((ka)^{1/3}\right) \tag{69}$$

$$\left|\Im\left(E_q^{A,\text{TM-CCFIO}}\right)\right| = \mathcal{O}\left((ka)^{1/3}\right) \tag{70}$$

$$\left|\Re\left(E_q^{A,\text{TE-CCFIO}}\right)\right| = \mathcal{O}\left((ka)^{1/3}\right) \tag{71}$$

$$\left|\Im\left(E_q^{A,\text{TE-CCFIO}}\right)\right| = \mathcal{O}\left((ka)^{1/3}\right). \tag{72}$$

IV. Current Error Analysis

This section aims at studying the consequences of the high-frequency behaviors of the aliasing spectral errors presented in Section III on the current errors, measuring the difference between the solutions of the integral equations (7)–(12) and the currents resulting from the solution of the BEM systems (13)–(18). These two currents will be denoted, respectively, as J and $\hat{J}$.

The excitation considered is the plane wave traveling along the x-axis [44], [56]. From the Mie scattering solution, the value J_n of the current J evaluated at the point with polar coordinates (a, ϕ_n) can be written as [44], [56]

$$J_n = \sum_{q=-\infty}^{\infty} U_q\, e^{-\mathrm{j}q\phi_n} \tag{73}$$

where U_q is given by

$$U_q^{\text{TM}} = \frac{2\mathrm{j}^{-q}}{\pi\eta ka\, H_q^{(2)}(ka)} \tag{74}$$

$$U_q^{\text{TE}} = \frac{2\mathrm{j}^{-q}}{\pi\eta ka\, H_q^{(2)'}(ka)}. \tag{75}$$

Similarly, the current resulting from the solution of one of the BEM linear systems evaluated at the point (a, ϕ_n), corresponding to the nth element of the array $\hat{\boldsymbol{J}}$, is denoted as $\hat{J}_n$ and can be written as

$$\hat{J}_n = \sum_{q=-\infty}^{\infty} \hat{U}_q\, e^{-\mathrm{j}q\phi_n}. \tag{76}$$

The difference between the solution of the integral equation and the solution of the linear system is denoted as ΔJ. The value ΔJ_n of ΔJ at (a, ϕ_n) is the difference between $\hat{J}_n$, representing the solution of the discrete problem, and J_n, representing the solution of the continuous problem at the point (a, ϕ_n). After defining the relative error coefficient υ_q as $\upsilon_q \coloneqq (\hat{U}_q - U_q)/U_q$, we expand the difference as

$$\Delta J_n = \hat{J}_n - J_n = \sum_{q=-\infty}^{\infty} U_q \upsilon_q\, e^{-\mathrm{j}q\phi_n}. \tag{77}$$

For the EFIE, the υ_q coefficient reads [44], [56]

$$\upsilon_q^{\text{TM/TE-EFIE}} = \frac{F_{-q}\left(1 - F_q\right) - E_q^{A,\mathcal{S}^k/\mathcal{N}^k}}{1 + E_q^{\mathcal{S}^k/\mathcal{N}^k}}. \tag{78}$$

By following similar steps as in [56], that is, by expressing the solution of the discrete problem as the ratio between the Fourier mode expansions of the right- and left-hand sides (RHS and LHS), for the MFIE, we have:

$$\upsilon_q^{\text{TX-MFIE}} = \frac{F_{-q}\left(1 - F_q\right) - E_q^{A,\text{TX-MFIO}^k}}{1 + E_q^{\text{TX-MFIO}^k}}. \tag{79}$$

To determine the current error in the CCFIE case, we sum the Fourier coefficients of the two components of the RHS tested with pyramid basis functions and divide the result by the Fourier coefficients of the discretization of the operator. The derivation, omitted for the sake of brevity, leads to the definition of $\upsilon_q^{\text{CCFIE}}$ as

$$\upsilon_q^{\text{TX-CCFIE}} = \frac{\hat{\lambda}_q^{\text{TX-CEFIO}}\upsilon_q^{\text{TX-EFIE}} + \hat{\lambda}_q^{\text{TX-CMFIO}}\upsilon_q^{\text{TX-MFIE}}}{\hat{\lambda}_q^{\text{TX-CEFIO}} + \hat{\lambda}_q^{\text{TX-CMFIO}}}. \tag{80}$$

A. Current Error Measures

Different measures of the current error are possible. We consider the L^2-measure

$$r_{L^2(\Gamma)} \coloneqq \left(\frac{\sum_{q=-\infty}^{\infty}\left|U_q\upsilon_q\right|^2}{\sum_{q=-\infty}^{\infty}\left|U_q\right|^2}\right)^{1/2} \tag{81}$$

the measure in the standard norm of the current space $H^s(\Gamma)$, with $s = \mp 1/2$ for the TM/TE formulations

$$r_{H^s(\Gamma)} \coloneqq \left(\frac{\sum_{q=-\infty}^{\infty}\left|U_q\upsilon_q\right|^2\left(1+q^2\right)^s}{\sum_{q=-\infty}^{\infty}\left|U_q\right|^2\left(1+q^2\right)^s}\right)^{1/2} \tag{82}$$

and the measure in a different norm in $H^s(\Gamma)$

$$r_{H_k^s(\Gamma)} \coloneqq \left(\frac{\sum_{q=-\infty}^{\infty}\left|U_q\upsilon_q\right|^2\left((ka)^2+q^2\right)^s}{\sum_{q=-\infty}^{\infty}\left|U_q\right|^2\left((ka)^2+q^2\right)^s}\right)^{1/2} \tag{83}$$

commonly used in high-frequency scattering applications [26], [59]. Another common error measure is the one in the $|\cdot|_{P^{\text{TM/TE}}}$ seminorm [60]

$$r_{P^{\text{TM/TE}}(\Gamma)} \coloneqq \left|\frac{\sum_{q=-\infty}^{\infty}\left|U_q\upsilon_q\right|^2\alpha_q^{\text{TM/TE}}}{\sum_{q=-\infty}^{\infty}\left|U_q\right|^2\alpha_q^{\text{TM/TE}}}\right|^{1/2} \tag{84}$$

where

$$\alpha_q^{\text{TM}} = \frac{k\eta\pi a}{2} J_q(ka)\, H_q^{(2)}(ka) \tag{85}$$

$$\alpha_q^{\text{TE}} = \frac{k\eta\pi a}{2} J_q'(ka)\, H_q^{(2)\prime}(ka). \tag{86}$$

Given the expressions (85) and (86) and the eigenvalues of the single-layer and hypersingular operators (21) and (23), (84) corresponds to

$$r_{P^{\text{TM}}(\Gamma)} = \left|\frac{\left(\mathcal{S}^k\Delta J, \Delta J\right)_{L^2(\Gamma)}}{\left(\mathcal{S}^k J, J\right)_{L^2(\Gamma)}}\right|^{1/2} \tag{87}$$

$$r_{P^{\text{TE}}(\Gamma)} = \left|\frac{\left(\mathcal{N}^k\Delta J, \Delta J\right)_{L^2(\Gamma)}}{\left(\mathcal{N}^k J, J\right)_{L^2(\Gamma)}}\right|^{1/2} \tag{88}$$

which can be approximated on any geometry as

$$\tilde{r}_{P^{\text{TM}}(\Gamma)} \coloneqq \left|\frac{\left(\hat{\boldsymbol{J}} - \boldsymbol{J}\right)^{\mathrm{T}}\boldsymbol{S}^k\left(\hat{\boldsymbol{J}} - \boldsymbol{J}\right)}{\boldsymbol{J}^{\mathrm{T}}\boldsymbol{S}^k\boldsymbol{J}}\right|^{1/2} \simeq r_{P^{\text{TM}}(\Gamma)} \tag{89}$$

$$\tilde{r}_{P^{\mathrm{TE}}(\Gamma)} := \left| \frac{\left(\hat{\boldsymbol{J}} - \boldsymbol{J}\right)^{\mathrm{T}} \boldsymbol{N}^k \left(\hat{\boldsymbol{J}} - \boldsymbol{J}\right)}{\boldsymbol{J}^{\mathrm{T}} \boldsymbol{N}^k \boldsymbol{J}} \right|^{1/2} \simeq r_{P^{\mathrm{TE}}(\Gamma)} \tag{90}$$

where $\boldsymbol{J}$ is the array of coefficients of the expansion of the current J in the pyramid functional space.

As a general remark, notice that, differently from the $H_k^s(\Gamma)$ norm [59], the $|\cdot|_{P^{\mathrm{TM/TE}}}$ seminorm does not preserve the balance between lower and higher derivatives. Indeed, the higher derivatives of the current, corresponding to spectral coefficients in the transition region, are scaled by factors which are $\mathcal{O}(ka)^{1/3}$ or $\mathcal{O}(ka)^{-1/3}$ for the TM/TE formulations, respectively. Hence, their relative importance with respect to lower derivatives, corresponding to spectral indices in the hyperbolic region, increases/decreases in frequency as $(ka)^{\pm 1/3}$.

In addition, while the $P^{\mathrm{TM/TE}}$ seminorm is equivalent to the H^s and to the H_k^s norms with respect to the discretization parameter h, it is not equivalent to them with respect to the frequency [59], [60], i.e.,

$$c_1(k)\ |u|_{P^{\mathrm{TM/TE}}} \leq \|u\|_{H^{\mp 1/2}} \leq c_2(k)\ |u|_{P^{\mathrm{TM/TE}}} \tag{91}$$

where the parameters c_1 and c_2 are not bounded in frequency. For these reasons, the $P^{\mathrm{TM/TE}}$ seminorm will not be considered further in this work.

B. High-Frequency Analysis of the Current Error

The coefficient $|U_q|^2$ in (81)–(83) is a nonoscillating function of the spectral index q. $|U_q^{\mathrm{TM}}|^2$ scales as $(ka)^{-1}$ in the hyperbolic region and as $(ka)^{-4/3}$ in the transition region; conversely, $|U_q^{\mathrm{TE}}|^2$ scales as $(ka)^{-1}$ in the hyperbolic region and as $(ka)^{-2/3}$ in the transition region. Moreover, it decays to zero in the elliptic region, making the contributions of the summations corresponding to indices $|q| \gg ka$ negligible, so that we safely restrict our analysis to the contributions in the hyperbolic and transition regions.

From the spectral analyses above, we infer that $|\upsilon_q^{\mathrm{TM\text{-}EFIE}}|$ and $|\upsilon_q^{\mathrm{TX\text{-}MFIE}}|$ have a constant behavior in the high-frequency limit, both in the hyperbolic and transition regions. As a consequence, the current relative error of the corresponding formulations is expected to be bounded in the high-frequency regime.

Differently, the increase of $|E_q^{A,\mathcal{N}^k}|$ as $(ka)^{1/3}$ in the high-frequency limit leads to an increase of $|\upsilon_q^{\mathrm{TE\text{-}EFIE}}|$ in the transition region at the same rate. The absence of lossy terms in the electric field equation (i.e., the kernel involved is the lossless Green's function G^k) results in a spectral shape invariance in frequency, so that the number of eigenvalues of $\mathcal{N}^k$ decaying in modulus as $(ka)^{-1/3}$ is proportional to the frequency. Hence, in (81), $\sum_{q=-\infty}^{\infty} |U_q \upsilon_q|^2$ can be seen as the sum of $\mathcal{O}(ka)$ terms in the transition region behaving as $(ka)^{-2/3} \cdot (ka)^{2/3}$ and of $\mathcal{O}(ka)$ terms in the hyperbolic region behaving as $(ka)^{-1} \cdot (ka)^0$, from which $\sum_{q=-\infty}^{\infty} |U_q \upsilon_q|^2 = \mathcal{O}(ka)$. Similarly for the denominator in (81), $\sum_{q=-\infty}^{\infty} |U_q|^2$, which approximately corresponds to the summation of $\mathcal{O}(ka)$ terms in the transition region behaving as $(ka)^{-2/3}$ and of $\mathcal{O}(ka)$ terms in the hyperbolic region behaving as $(ka)^{-1}$, from which $\sum_{q=-\infty}^{\infty} |U_q|^2 = \mathcal{O}((ka)^{1/3})$. Finally, when considering the TE-EFIE, the error measure $r_{L^2(\Gamma)}$ increases asymptotically as $(ka)^{1/3}$ in the high-frequency limit. By following a similar reasoning, the high-frequency behavior as $(ka)^{1/3}$ of $r_{H^s(\Gamma)}$ and $r_{H_k^s(\Gamma)}$ for the TE-EFIE can be shown.

In the TM-CCFIE case, the error contribution $\upsilon_q^{\mathrm{TM\text{-}CCFIE}}$ is given by the weighted average between the two contributions $\upsilon_q^{\mathrm{TM\text{-}EFIE}}$ and $\upsilon_q^{\mathrm{TM\text{-}MFIE}}$, which are bounded in the high-frequency limit. Hence, in this case, the increasing spectral error does not result in an increasing current error, as the increasing behavior of $|E_q^{A,\mathcal{N}^k}|$ in frequency only impacts the relative importance of $\upsilon_q^{\mathrm{TM\text{-}EFIE}}$ and $\upsilon_q^{\mathrm{TM\text{-}MFIE}}$ with respect to each other: the spectral deformation induced by the preconditioning does not induce any deterioration in the current accuracy. Moreover, we note that, even though the two error components $\upsilon_q^{\mathrm{TM\text{-}EFIE}}$ and $\upsilon_q^{\mathrm{TM\text{-}MFIE}}$ may present sharp peaks in correspondence of determined indices $q_{\mathrm{res,TM\text{-}EFIE}}$ and $q_{\mathrm{res,TM\text{-}MFIE}}$ at the resonance frequencies of the TM-EFIE and TM-MFIE, the current error of the TM-CCFIE is immune from spurious resonances as a result of the weighted average in favor of $\upsilon_q^{\mathrm{TM\text{-}MFIE}}$ at indices $q_{\mathrm{res,TM\text{-}EFIE}}$ and in favor of $\upsilon_q^{\mathrm{TM\text{-}EFIE}}$ at indices $q_{\mathrm{res,TM\text{-}MFIE}}$.

The analysis is more complicated in the TE-CCFIE case. At first, we notice that the presence of lossy contributions in the equation (i.e., the presence of the complex $\tilde{k}$ in the kernel of the preconditioning operators) determines a spectral deformation in frequency. For spectral indices in the transition region, the weighted average with oscillating weights alleviates the effect of the high-frequency increase of $|\upsilon_q^{\mathrm{TE\text{-}EFIE}}|$ over $|\upsilon_q^{\mathrm{TE\text{-}CCFIE}}|$. Hence, we expect the current error of the TE-CCFIE to increase in the high-frequency limit at a rate equal to or slower than $(ka)^{1/3}$. Numerical results in Section VII indicate a substantial improvement of the current error increase rate of the TE-CCFIE with respect to the TE-EFIE.

V. Scattering Error Analysis

Given the same plane-wave excitation as above, the electric (for TM polarization) or magnetic (for TE polarization) scattered field in the longitudinal direction is proportional to the scattering parameter [56]

$$S(\phi) = \sum_{q=-\infty}^{\infty} R_q e^{-\mathrm{j}q\phi} \tag{92}$$

where the expression of the Fourier coefficients R_q for the two polarizations is

$$R_q^{\mathrm{TM}} = J_q(ka) / H_q^{(2)}(ka) \tag{93}$$

$$R_q^{\mathrm{TE}} = J_q'(ka) / H_q^{(2)\prime}(ka). \tag{94}$$

In particular, for the TM polarization, the electric far-field scattered by the longitudinal current $\boldsymbol{J}_z$ at the point at polar coordinates (r_{FF}, ϕ) for $r_{\mathrm{FF}} \gg a$ is

$$\boldsymbol{E}(r_{\mathrm{FF}}, \phi) \simeq -\sqrt{\frac{2\mathrm{j}}{\pi k r_{\mathrm{FF}}}} e^{-\mathrm{j}kr_{\mathrm{FF}}} S^{\mathrm{TM}}(\phi)\, \hat{\boldsymbol{z}} \tag{95}$$

where the far-field approximation [2, eq. 2.3.17] and the large-argument expansion of the Hankel function [38, eq. 9.2.4] have

been applied. Similarly, for the TE polarization, by applying equivalent approximations, the far-field magnetic field reads

$$\boldsymbol{H}(r_{\mathrm{FF}},\phi) \simeq -\frac{1}{\mathrm{j}\eta}\sqrt{\frac{2\mathrm{j}}{\pi k r_{\mathrm{FF}}}}e^{-\mathrm{j}kr_{\mathrm{FF}}}S^{\mathrm{TE}}(\phi)\,\hat{z}. \tag{96}$$

The far-field electric and magnetic fields resulting from the numerical solution of the discrete TM and TE formulations can be written as [56]

$$\hat{\boldsymbol{E}}(r_{\mathrm{FF}},\phi) \simeq -\sqrt{\frac{2\mathrm{j}}{\pi k r_{\mathrm{FF}}}}e^{-\mathrm{j}kr_{\mathrm{FF}}}\hat{S}^{\mathrm{TM}}(\phi)\,\hat{z} \tag{97}$$

$$\hat{\boldsymbol{H}}(r_{\mathrm{FF}},\phi) \simeq -\frac{1}{\mathrm{j}\eta}\sqrt{\frac{2\mathrm{j}}{\pi k r_{\mathrm{FF}}}}e^{-\mathrm{j}kr_{\mathrm{FF}}}\hat{S}^{\mathrm{TE}}(\phi)\,\hat{z} \tag{98}$$

where

$$\hat{S}(\phi) \coloneqq \sum_{q=-\infty}^{\infty}\hat{R}_q e^{-\mathrm{j}q\phi}. \tag{99}$$

After defining the relative error coefficient ρ_q as $\rho_q \coloneqq (\hat{R}_q - R_q)/R_q$, we expand the difference between the numerical scattering resulting from the solution of the discrete equations and the exact one as

$$\hat{S}(\phi) - S(\phi) = \sum_{q=-\infty}^{\infty} R_q\rho_q e^{-\mathrm{j}q\phi}. \tag{100}$$

From the Fourier mode expansion of the scattering operator, the error coefficient is given by

$$\rho_q = F_q\left(\upsilon_q + 1\right) - 1. \tag{101}$$

Hence, for the EFIE, the ρ_q coefficient reads [56]

$$\rho_q^{\mathrm{TM/TE\text{-}EFIE}} = -\frac{E_q^{A,\mathcal{S}^k/\mathcal{N}^k}}{1 + E_q^{\mathcal{S}^k/\mathcal{N}^k}} \tag{102}$$

and, for the MFIE, it reads

$$\rho_q^{\mathrm{TX\text{-}MFIE}} = -\frac{E_q^{A,\mathrm{TX\text{-}MFIO}^k}}{1 + E_q^{\mathrm{TX\text{-}MFIO}^k}}. \tag{103}$$

In the CCFIE case, ρ_q^{CCFIE} can be derived from the definition of $\upsilon_q^{\mathrm{CCFIE}}$ and (101), resulting in the expression

$$\rho_q^{\mathrm{TX\text{-}CCFIE}} = \frac{\hat{\lambda}_q^{\mathrm{TX\text{-}CEFIO}}\rho_q^{\mathrm{TX\text{-}EFIE}} + \hat{\lambda}_q^{\mathrm{TX\text{-}CMFIO}}\rho_q^{\mathrm{TX\text{-}MFIE}}}{\hat{\lambda}_q^{\mathrm{TX\text{-}CEFIO}} + \hat{\lambda}_q^{\mathrm{TX\text{-}CMFIO}}}. \tag{104}$$

A. Scattering Error Measure

We define the scattering relative error as

$$s_{L^2(\Gamma_{\mathrm{FF}})} \coloneqq \left(\frac{\sum_{q=-\infty}^{\infty}\left|R_q\rho_q\right|^2}{\sum_{q=-\infty}^{\infty}\left|R_q\right|^2}\right)^{1/2}. \tag{105}$$

Note that, given the definition of the coefficient R_q [see (93) and (94)] and that of the coefficient U_q [see (74) and (75)], s_{L^2} can also be written, for the two polarizations, as

$$s^{\mathrm{TM}}_{L^2(\Gamma_{\mathrm{FF}})} \coloneqq \left(\frac{\sum_{q=-\infty}^{\infty}\left|U_q^{\mathrm{TM}}J_q(ka)\rho_q\right|^2}{\sum_{q=-\infty}^{\infty}\left|U_q^{\mathrm{TM}}J_q(ka)\right|^2}\right)^{1/2} \tag{106}$$

$$s^{\mathrm{TE}}_{L^2(\Gamma_{\mathrm{FF}})} \coloneqq \left(\frac{\sum_{q=-\infty}^{\infty}\left|U_q^{\mathrm{TE}}J'_q(ka)\rho_q\right|^2}{\sum_{q=-\infty}^{\infty}\left|U_q^{\mathrm{TE}}J'_q(ka)\right|^2}\right)^{1/2}. \tag{107}$$

B. High-Frequency Analysis of the Scattering Error

By following the same reasoning as in Section IV, given the high-frequency behavior of the aliasing spectral error of the operators in the transition region, the scattering error is expected to behave as $\mathcal{O}(1)$ for the TM-EFIE, TM-MFIE, and TE-MFIE, and as $\mathcal{O}((ka)^{1/3})$ for the TE-EFIE in the high-frequency limit. Moreover, as the scattering error of the TM-CCFIE depends on the weighted average between $\rho_q^{\mathrm{TM\text{-}EFIE}}$ and $\rho_q^{\mathrm{TM\text{-}MFIE}}$, bounded in the high-frequency limit, it is expected to be bounded in the high-frequency regime, similar to the current error. On the other hand, an increase of the scattering error at a rate at most equal to $(ka)^{1/3}$ is expected from the solution of the TE-CCFIE due to the increasing behavior of $\rho_q^{\mathrm{TE\text{-}EFIE}}$ as $(ka)^{1/3}$ in the transition region in the high-frequency limit.

As an aside, it is worth noting that the presence of the coefficients $|J_q(ka)|^2$ and $|J'_q(ka)|^2$ in the definition of $s^{\mathrm{TM}}_{L^2(\Gamma_{\mathrm{FF}})}$ (106) and $s^{\mathrm{TE}}_{L^2(\Gamma_{\mathrm{FF}})}$ (107) affects the sensitivity of the scattering error to spurious resonances differently for different formulations. Indeed, since the zeros of $J_q(ka)$ and $J'_q(ka)$ determine the resonances of the TM-EFIE and TE-EFIE, respectively, we expect that the coefficient $|\rho_q|^2$ at the resonant indices $q_{\mathrm{res,TM\text{-}EFIE}}$ and $q_{\mathrm{res,TE\text{-}EFIE}}$ will be attenuated by $|J_q(ka)|^2$ and $|J'_q(ka)|^2$, approaching the zero at the same indices. This results, when solving the EFIE, in a scattering error that is quasi-immune to spurious resonances, as reported in the literature [61], [62], [63]. The contributions $|J_q(ka)|^2$ and $|J'_q(ka)|^2$, beneficial for the scattering from the EFIE, become detrimental in the MFIE case instead. Indeed, the resonant indices $q_{\mathrm{res,TM\text{-}MFIE}}$ and $q_{\mathrm{res,TE\text{-}MFIE}}$, at which the coefficients $|\rho_q|^2$ are expected to reach local maxima, are determined by the zeros of $J'_q(ka)$ and $J_q(ka)$, respectively. Given the oscillatory nature of the Bessel function $J_q(ka)$, at these resonance indices, the functions $J_q(ka)$ and $J'_q(ka)$, respectively, achieve their local maxima, leading to an amplification of the detrimental effect of spurious resonances over the scattering error from the TM- and TE-MFIE.

VI. Overcoming the Pollution Effect by Filtering

By restricting our analysis to the cylindrical case, we lose generality, but we gain a powerful model to explain the mechanism of discretization of integral operators by using BEM and its consequences. As the aliasing spectral error of the hypersingular operator is responsible for the increasing behavior of the current and scattering errors delineated in Sections IV and V, we believe that spectral operator filtering strategies, such as the ones presented in [36], may significantly attenuate, or even solve, the pollution problem. They consist of the definition of a spectrally truncated modification of the Green's function, which can be numerically approximated with low computational complexity and employed in the kernel of the newly defined, filtered operators.

To showcase this idea, we will consider the ideally filtered operator $\mathcal{N}_F^k$ with eigenvalues

$$\lambda_q^{\mathcal{N}_F^k} = \begin{cases}\lambda_q^{\mathcal{N}^k}, & \text{if } |q| \le q_{lim}\\ 0, & \text{otherwise.}\end{cases} \tag{108}$$

The choice of the cutoff spectral index

$$q_{\text{lim}} = \lfloor (n_\lambda - 1 - \epsilon)\, ka \rfloor \tag{109}$$

with $\epsilon > 0$ allows the suppression of the aliasing spectral error in both the hyperbolic and the transition regions of the spectra, as is clear from (30). Hence, in the transition region in the high-frequency limit, we obtain

$$\left|\Re\left(E_q^{\mathcal{N}_F^k}\right)\right| = \mathcal{O}(1)\,, \quad \left|\Im\left(E_q^{\mathcal{N}_F^k}\right)\right| = \mathcal{O}(1) \tag{110}$$

which, in turn, results in a bounded spectral error of the operators TM-CCFIO$_F$ and TE-CCFIO$_F$, with expressions given by the ones of the respective nonfiltered ones where $\mathcal{N}^k$ is substituted by $\mathcal{N}_F^k$ and $\mathcal{N}^{\tilde{k}}$ is substituted by $\mathcal{N}_F^{\tilde{k}}$

$$\left|\Re\left(E_q^{\text{TM-CCFIO}_F^k}\right)\right| = \mathcal{O}(1)\,, \quad \left|\Im\left(E_q^{\text{TM-CCFIO}_F^k}\right)\right| = \mathcal{O}(1) \tag{111}$$

$$\left|\Re\left(E_q^{\text{TE-CCFIO}_F^k}\right)\right| = \mathcal{O}(1)\,, \quad \left|\Im\left(E_q^{\text{TE-CCFIO}_F^k}\right)\right| = \mathcal{O}(1)\,. \tag{112}$$

The bounded-in-frequency spectral error of the filtered formulations leads, in turn, to a bounded current and scattering error. To estimate the practical impact of filtering, we evaluate the current and spectral error resulting from the solution of the TE-EFIE$_F$, in which we have substituted the operator $\mathcal{N}^k$ with $\mathcal{N}_F^k$, and of the TE-CCFIE$_F$. The results of this analysis are reported in Section VII.

VII. Numerical Results

The numerical results presented in this section are intended to demonstrate the convergence between the numerical results from our BEM implementation and what is predicted from theory, as well as to numerically verify the high-frequency behavior of the spectral, current, and scattering errors. The BEM matrices and RHSs have been obtained (in their nonsingular terms) by numerical integration exploiting standard Gauss–Legendre rules with a high number of integration points per mesh element (100), to minimize the integration error with respect to the discretization error which is the source of numerical error of interest in this contribution. The results predicted from our developments have been obtained by truncating the infinite sums in q to $q \in [-(N-1)/2, (N-1)/2]$ (with N odd) and by only considering the first harmonic term in the aliasing contribution, that is, limiting the infinite summation in (26) to the terms corresponding to $s = \{-1, 0, 1\}$. The only exception to this setting is in Fig. 2, in which two harmonics were taken into account, corresponding to the terms $s = \{-2, -1, 0, 1, 2\}$, in order to improve the convergence to numerical results. In general, a further improvement of convergence has been observed and is expected for higher numbers of harmonics, but numerical stability in the evaluation of special functions limits the analysis.

If not otherwise specified, the circular geometry under test is the one of the radius 1 m discretized at $n_\lambda = 4$. Given the circulant structure of the interaction matrices, the fast Fourier transform (FFT) algebra is employed to compute matrix-vector and diagonalization operations in linear complexity.

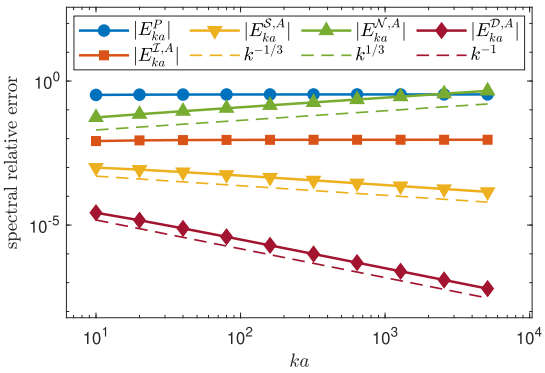

Fig. 1. Predicted values [from (30)] of projection and aliasing spectral error in the transition region for diverse operators for varying ka with $n_\lambda = 4$.

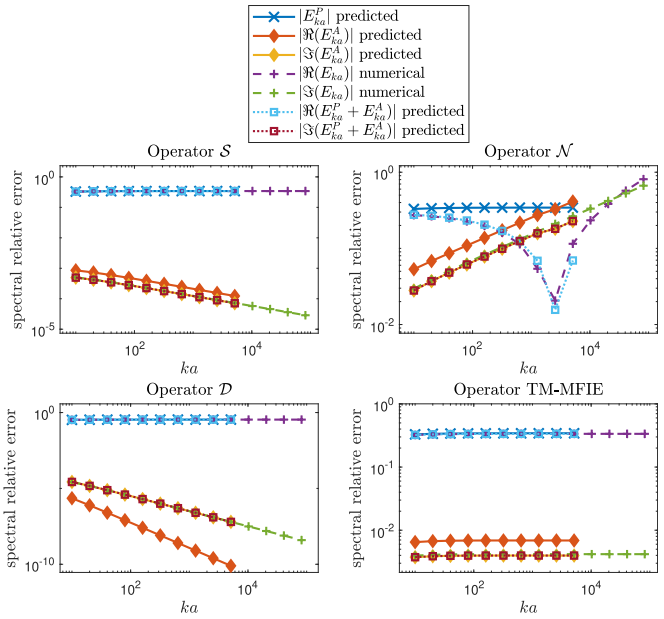

Fig. 2. Projection and aliasing spectral error in the transition region for diverse operators for varying ka with $n_\lambda = 4$. Comparison between the predicted values [from (30)] and numerical values from our BEM code.

A. Spectral Error Results

In the first set of numerical results, we analyze the high-frequency behavior of the spectral relative error of the four standard operators (30), to confirm that the trends predicted from the asymptotic expansions of the Bessel functions in Section III hold. Fig. 1 shows the predicted projection and aliasing contributions in absolute value for the operators $\mathcal{I}$, $\mathcal{S}$, $\mathcal{N}$, and $\mathcal{D}$, in the transition region, for $q = ka$ (with ka integer), obtained by evaluation of (30). The results confirm the predicted decrease as $(ka)^{-1/3}$ and as $(ka)^{-1}$ of $|E_{ka}^{A,\mathcal{S}}|$ and $|E_{ka}^{A,\mathcal{D}}|$ and the expected increase as $(ka)^{1/3}$ of $|E_{ka}^{A,\mathcal{N}}|$.

In Fig. 2, the analytically predicted and numerical spectral relative errors are compared—in real and imaginary components. We observe that the real part of E_{ka} obtained numerically corresponds in modulus to $|E_{ka}^{P}|$ (where E_{ka}^{P} is real) for $\mathcal{S}$, $\mathcal{D}$, and TM-MFIE operators. Instead, the imaginary part of E_{ka} corresponds to the imaginary part of the aliasing error contribution and decays in modulus as $(ka)^{-1/3}$ for $\mathcal{S}$,

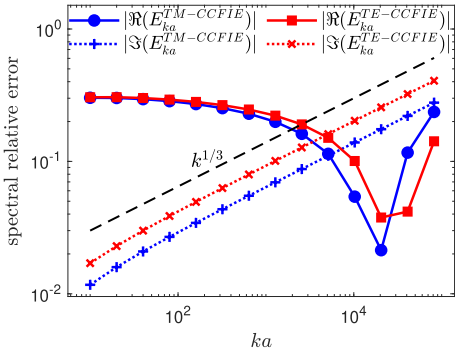

Fig. 3. Spectral error of the CCFIO in the transition region for varying ka with $n_\lambda = 4$. These results have been obtained numerically using our BEM code.

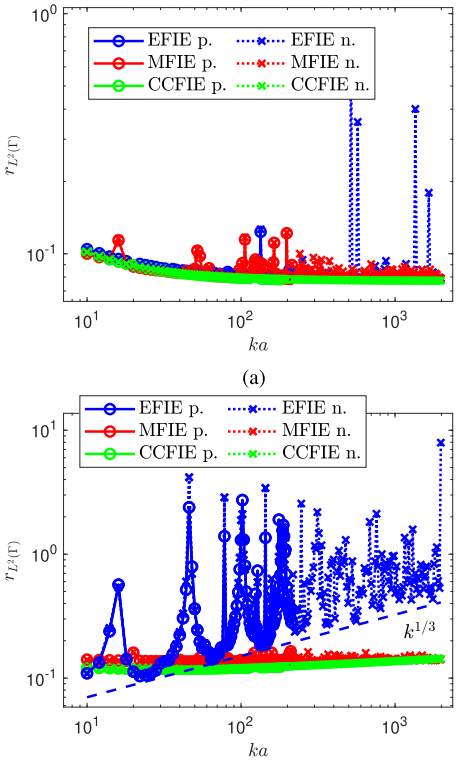

Fig. 4. Comparison between predicted (p.) and numerical (n.) results for the L_2 current error of (a) TM and (b) TE formulations for varying ka with $n_\lambda = 4$.

as $(ka)^{-1}$ for $\mathcal{D}$, and is bounded for the TM-MFIO. We also observe that the real part of the aliasing error contribution for operator $\mathcal{D}$ decays in modulus as $(ka)^{-5/3}$, following from the behavior of $|\Im(\lambda_q^{\mathcal{D}})|$ in the transition region as $(ka)^{-2/3}$. In the hypersingular operator case, the real part of the aliasing component contributes to the definition of the real spectral relative error. We observe that it is of opposite sign with respect to the projection component, resulting in an initial decrease of the sum, up to a cancellation in the frequency point at which $E_{ka}^{P} \simeq -\Re(E_{ka}^{A,\mathcal{N}})$. However, the asymptotic behavior of $E_{ka}^{\mathcal{N}}$ in both real and imaginary parts is determined by the aliasing error component, which increases in modulus as $(ka)^{1/3}$ in both real and imaginary components.

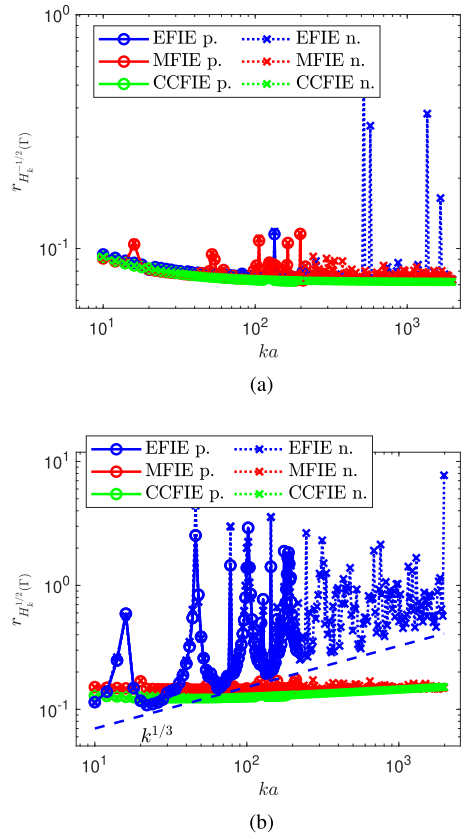

Fig. 5. Comparison between predicted (p.) and numerical (n.) results for the H_k^s current error of (a) TM and (b) TE formulations for varying ka with $n_\lambda = 4$.

The numerically obtained spectral relative error for the CCFIE operators is represented in Fig. 3, in real and imaginary components, and shows a behavior similar to the $\mathcal{N}$ operator: the imaginary component increases as $(ka)^{1/3}$, while the real part is subject to cancellation before increasing.

B. Current Error Results

To validate the estimates on the current error presented in Section IV, we first verify the convergence between our numerical results and predicted values for the diverse norms (81) and (83) in Figs. 4 and 5. All these scenarios show a good agreement between numerical and predicted results. The current error resulting from the solution of the TE-EFIE increases in the high-frequency regime as $(ka)^{1/3}$ away from resonances for all error measures, which is consistent with the theoretical expectations (Section IV-B). The solution of the TE-CCFIE provides a current error that increases in frequency at a rate lower than $(ka)^{1/3}$. In particular, this occurs despite the good conditioning properties of the CCFIOs, as summarized in Fig. 6.

C. Scattering Error Results

Our models for the scattering error are compared to numerical results in Fig. 7. In accordance with theoretical

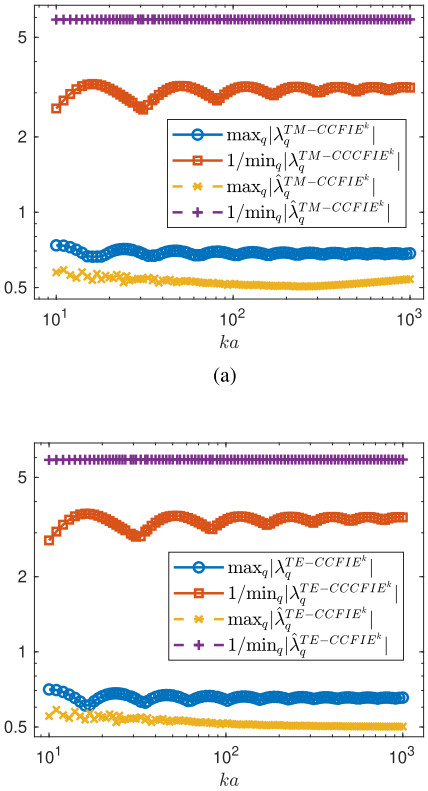

Fig. 6. L_2 norm of the CCFIO and its inverse, and L_2 norm of the CCFIO matrix evaluated with $n_\lambda = 4$ and its inverse, for (a) TM and (b) TE formulations.

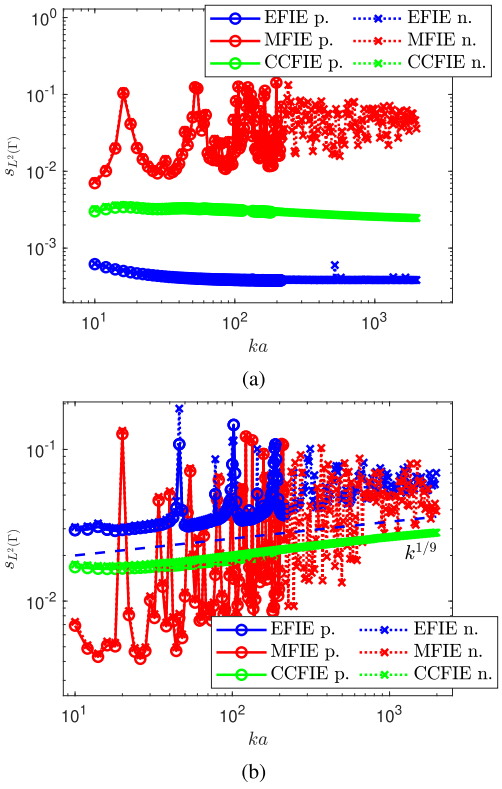

Fig. 7. Comparison between predicted (p.) and numerical (n.) results for the L_2 scattering error of (a) TM and (b) TE formulations for varying ka with $n_\lambda = 4$.

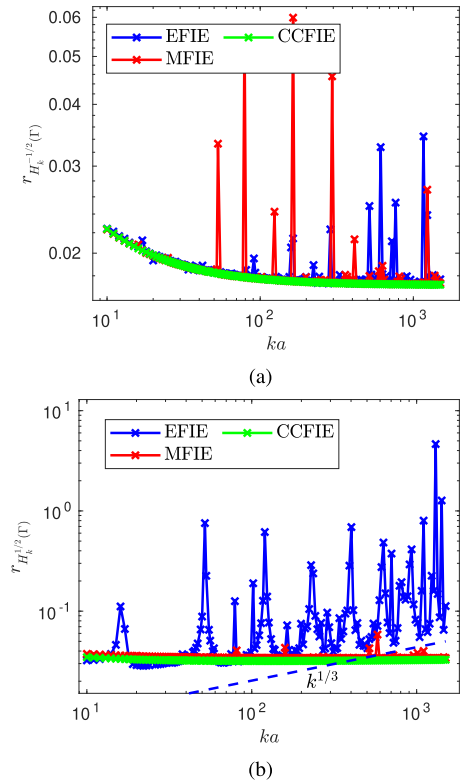

Fig. 8. Numerical results for the H_k^s current error of (a) TM and (b) TE formulations for varying ka with $n_\lambda = 8$.

expectations, the TM-EFIE provides a bounded scattering error, while both the TE-EFIE and the TE-CCFIE provide a scattering error that increases in the high-frequency regime. The increase rate is approximately equal to $(ka)^{1/9}$, compatible with the expectation of $\mathcal{O}((ka)^{1/3})$ (Section V-B).

Moreover, as expected from (106) and (107), in the MFIE case, we observe sharp peaks of the scattering error at the resonance frequencies. We also notice an increase of $s_{L^2(\Gamma)}$ toward high frequencies away from resonances, not compatible with the theoretical expectation of bounded scattering error reported in Section V. We believe this may be due to the detrimental effect of spurious resonances. On the other hand, the TE-EFIE also shows sharp error peaks at the resonant frequencies, while the TM-EFIE is more robust.

D. Influence of the Discretization Parameter n_λ

To investigate the influence of the discretization parameter n_λ on the current and scattering errors, we numerically estimate these quantities under the condition $n_\lambda = 8$ (Figs. 8 and 9). Both the current and scattering error resulting from the BEM discretization at $n_\lambda = 8$ are significantly lower than the ones achieved at $n_\lambda = 4$. In Fig. 8(b), we can still observe an asymptotic increase of the current error resulting from the TE-EFIE as $(ka)^{1/3}$ in the high-frequency regime, but in this case, the onset of the increasing behavior, preceded by a constant behavior, is at a higher value of ka than in the case of $n_\lambda = 4$. Also, the asymptotic increase of the scattering error from the TE-EFIE discretized at $n_\lambda = 8$,

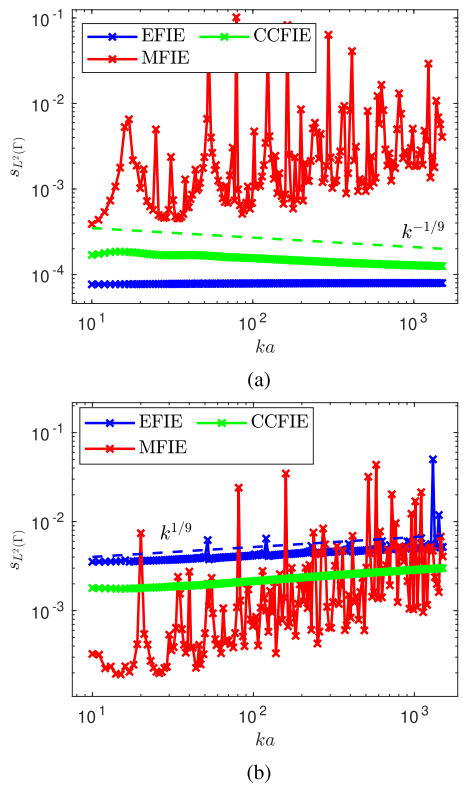

Fig. 9. Numerical results for the L_2 scattering error of (a) TM and (b) TE formulations for varying ka with $n_\lambda = 8$.

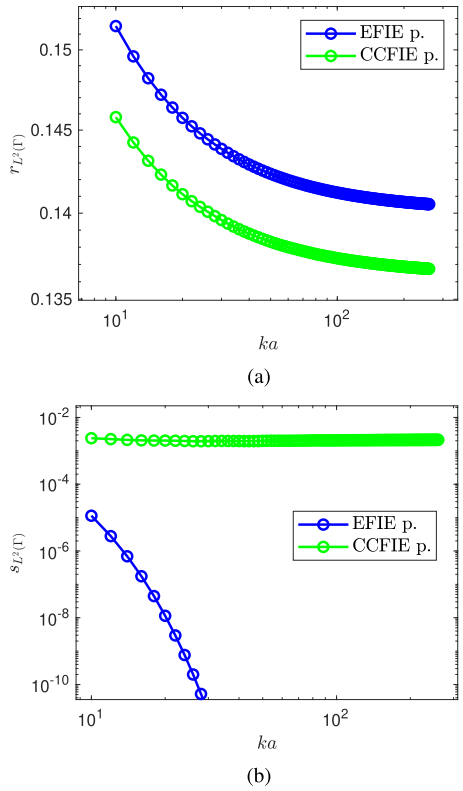

Fig. 10. (a) L_2 predicted current error and (b) L_2 predicted scattering error for the TE-EFIE and TE-CCFIE built with the ideally filtered operator $\mathcal{N}_F^k$ for varying ka with $n_\lambda = 4$.

shown in Fig. 9(b), is comparable with the one at $n_\lambda = 4$ [in Fig. 7(b)].

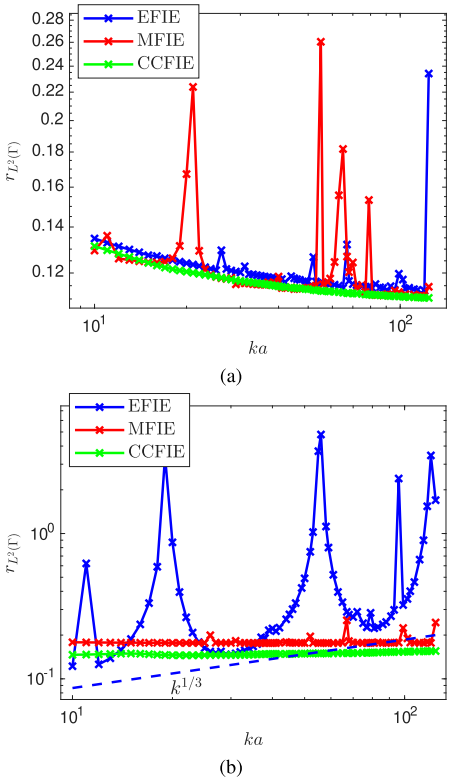

Fig. 11. Numerical results for the L_2 current error of (a) TM and (b) TE formulations for varying ka with $n_\lambda = 4$ applied over an elliptical boundary with a perimeter of $2\pi a$ and an aspect ratio of 2.

E. Proposed Filtering Approach

The proposed filtering approach has been applied to modify the TE-EFIE and TE-CCFIE by substituting the hypersingular operator $\mathcal{N}^k$ with the ideally filtered operator $\mathcal{N}_F^k$. The resulting current and scattering errors are shown in Fig. 10. From these figures, we note that the current error of the filtered formulations does not increase in frequency. This was expected, as the spectral error of the discretization of $\mathcal{N}_F^k$ and of all the operators involved in the TE-CCFIE$_F$ does not increase in the high-frequency regime.

Also, from the current error results, we immediately note the absence of the sharp increase of the current error in correspondence to resonance frequencies, as it is the case for the nonfiltered formulations. This highlights the importance of the aliasing spectral error components over the resonant and quasi-resonant modes of the hypersingular operator in the hyperbolic region and their roles in determining the above-mentioned peaks in the current error. The difference with respect to the TM-EFIE, resulting in milder peaks of current error in correspondence with resonance frequencies, is because the eigenvalues of the hypersingular operators increase in modulus as q toward high spectral indices, resulting in higher values of aliasing spectral error.

As far as the scattering error—which is less prone to the projection spectral error than the current error—is concerned, since the coefficient R_q decays in the elliptic region and since the error coefficient

$$\rho_q^{\text{TE-EFIE}_F} = -\frac{E_q^{A,\mathcal{N}_F^k}}{1 + E_q^{\mathcal{N}_F^k}} \tag{113}$$

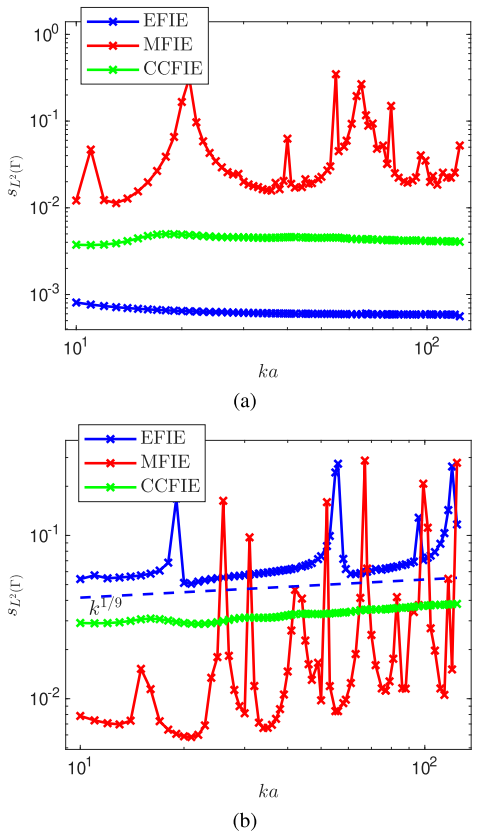

Fig. 12. Numerical results for the L_2 scattering error of (a) TM and (b) TE formulations for varying ka with $n_\lambda = 4$ applied over an elliptical boundary with a perimeter of $2\pi a$ and an aspect ratio of 2.

is exactly null in the hyperbolic and transition regions, the scattering error of the TE-EFIE$_F$ goes to zero, as shown in Fig. 10(b). On the other hand, the TE-CCFIE$_F$, differently from the TE-CCFIE, exhibits a bounded-in-frequency scattering error, stable at a value lower than the ones achieved by the nonfiltered counterpart.

F. Numerical Results Over the Elliptical Cross-Sectional Cylinder

The analysis reported so far over the circular cylinder is exact and allows for the clear identification of the root causes and consequences of the pollution phenomenon. Due to the nonnormality of boundary integral operators over noncircular domains [64], an expression similar to (26) would be challenging to obtain for noncircular boundaries. However, even nonorthogonal matrix decompositions derived from the Green's function expansion in some special coordinate systems, such as spherical [65] or elliptic systems, allow us to identify a pollution phenomenon resulting from the cross-interference between separate spectral contributions of the operators into the spectrum of the derived matrices.

The same effects can also be evidenced for noncircular boundaries with standard BEM codes, for instance, using pyramid basis-function-based BEM discretization. In the following, we use such a code to study an elliptical cross-sectional cylinder with boundary $\Gamma_{\text{ell.}}$ of aspect ratio 2 and length $2\pi a$. Figs. 11 and 12 show current and scattering errors for the six formulations that are comparable with the ones obtained over the circular cylinder. These results show that pollution is indeed affecting some of the formulations and can also be observed without relying on analytic techniques.

VIII. Conclusion

In this contribution, we analyzed several widely used BIEs for the electromagnetic scattering problem from the canonical cylinder discretized via the BEM. From the closed-form expressions for spectral, current, and scattering errors, we identified a form of pollution affecting some of them, that is, when increasing the frequency and keeping the product kh constant (i.e., in the high-frequency regime), the spectral and solution errors increase. The proposed analysis has the power to clearly identify the roots of this phenomenon and allows us to take the first step toward its solution or mitigation. This study is corroborated by excellent agreement between theoretical findings and numerical results from our in-house BEM solver.

References

[1] R. F. Harrington, *Field Computation by Moment Methods*. Hoboken, NJ, USA: Wiley, May 1993.
[2] J.-M. Jin, *Theory and Computation of Electromagnetic Fields*, 2nd ed., Piscataway, NJ, USA: IEEE Press, 2015.
[3] O. Steinbach, *Numerical Approximation Methods for Elliptic Boundary Value Problems: Finite and Boundary Elements*. New York, NY, USA: Springer, 2008.
[4] I. Babuska, F. Ihlenburg, E. T. Paik, and S. A. Sauter, "A generalized finite element method for solving the Helmholtz equation in two dimensions with minimal pollution," *Comput. Methods Appl. Mech. Eng.*, vol. 128, nos. 3–4, pp. 325–359, Dec. 1995.
[5] H. Weyl, "Das asymptotische verteilungsgesetz der eigenwerte linearer partieller differentialgleichungen (mit einer anwendung auf die theorie der Hohlraumstrahlung)," *Mathematische Annalen*, vol. 71, no. 4, pp. 441–479, Dec. 1912.
[6] M. Gustafsson, "Degrees of freedom for radiating systems," *IEEE Trans. Antennas Propag.*, vol. 73, no. 2, pp. 1028–1038, Feb. 2025.
[7] C. E. Shannon, "Communication in the presence of noise," *Proc. IRE*, vol. 37, no. 1, pp. 10–21, Jan. 1949.
[8] I. G. Graham, M. Löhndorf, J. M. Melenk, and E. A. Spence, "When is the error in the h-BEM for solving the Helmholtz equation bounded independently of k?," *BIT Numer. Math.*, vol. 55, no. 1, pp. 171–214, Mar. 2015.
[9] J. Galkowski, "Lower bounds for piecewise polynomial approximations of oscillatory functions," *J. Approximation Theory*, vol. 305, Jan. 2025, Art. no. 106100.
[10] A. Bayliss, C. I. Goldstein, and E. Turkel, "On accuracy conditions for the numerical computation of waves," *J. Comput. Phys.*, vol. 59, no. 3, pp. 396–404, Jul. 1985.
[11] A. K. Aziz, R. B. Kellogg, and A. B. Stephens, "A two point boundary value problem with a rapidly oscillating solution," *Numerische Math.*, vol. 53, nos. 1–2, pp. 107–121, Jan. 1988.
[12] F. Ihlenburg and I. Babuska, "Finite element solution of the Helmholtz equation with high wave number part I: The H-version of the FEM," *Comput. Math. Appl.*, vol. 30, no. 9, pp. 9–37, Nov. 1995.
[13] F. Ihlenburg and I. Babuska, "Dispersion analysis and error estimation of Galerkin finite element methods for the Helmholtz equation," *Int. J. Numer. Methods Eng.*, vol. 38, no. 22, pp. 3745–3774, Nov. 1995.
[14] I. Babuska, F. Ihlenburg, T. Strouboulis, and S. K. Gangaraj, "Aposteriori error estimation for finite element solutions of Helmholtz' equation—Part II: Estimation of the pollution error," *Int. J. Numer. Methods Eng.*, vol. 40, no. 21, pp. 3883–3900, Nov. 1997.
[15] I. M. Babuska and S. A. Sauter, "Is the pollution effect of the FEM avoidable for the Helmholtz equation considering high wave numbers?," *SIAM J. Numer. Anal.*, vol. 34, no. 6, pp. 2392–2423, Dec. 1997.
[16] I. Babuška and J. M. Melenk, "The partition of unity method," *Int. J. Numer. Methods Eng.*, vol. 40, pp. 727–758, Feb. 1997.

[17] K. Wang and Y. Wong, "Pollution-free finite difference schemes for non-homogeneous Helmholtz equation," *Int. J. Numer. Anal. Model.*, vol. 11, no. 4, pp. 787–815, 2014.

[18] L. P. Franca, C. Farhat, A. P. Macedo, and M. Lesoinne, "Residual-free bubbles for the Helmholtz equation," *Int. J. Numer. Methods Eng.*, vol. 40, no. 21, pp. 4003–4009, Nov. 1997.

[19] L. L. Thompson and P. M. Pinsky, "A Galerkin least-squares finite element method for the two-dimensional Helmholtz equation," *Int. J. Numer. Methods Eng.*, vol. 38, no. 3, pp. 371–397, Feb. 1995.

[20] F. Ihlenburg and I. Babuska, "Finite element solution of the Helmholtz equation with high wave number part II: The h-p version of the FEM," *SIAM J. Numer. Anal.*, vol. 34, no. 1, pp. 315–358, Feb. 1997.

[21] A. Deraemaeker, I. Babu?ka, and P. Bouillard, "Dispersion and pollution of the FEM solution for the Helmholtz equation in one, two and three dimensions," *Int. J. Numer. Methods Eng.*, vol. 46, no. 4, pp. 471–499, Oct. 1999.

[22] T. Betcke, E. van'T Wout, and P. Gélat, "Computationally efficient boundary element methods for high-frequency Helmholtz problems in unbounded domains," in *Modern Solvers for Helmholtz Problems*, D. Lahaye, J. Tang, and K. Vuik, Eds., Cham, Switzerland: Springer, 2017, pp. 215–243.

[23] S. Marburg, "Six boundary elements per wavelength: Is that enough?," *J. Comput. Acoust.*, vol. 10, no. 1, pp. 25–51, Mar. 2002.

[24] S. Chaillat, M. Darbas, and F. L. Louër, "Fast iterative boundary element methods for high-frequency scattering problems in 3D elastodynamics," *J. Comput. Phys.*, vol. 341, pp. 429–446, Jul. 2017.

[25] H. Barucq, A. Bendali, M. Fares, V. Mattesi, and S. Tordeux, "A symmetric trefftz-DG formulation based on a local boundary element method for the solution of the Helmholtz equation," *J. Comput. Phys.*, vol. 330, pp. 1069–1092, Feb. 2017.

[26] J. Galkowski and E. A. Spence, "Does the Helmholtz boundary element method suffer from the pollution effect?," *SIAM Rev.*, vol. 65, no. 3, pp. 806–828, Aug. 2023.

[27] S. Marburg, "A pollution effect in the boundary element method for acoustic problems," *J. Theor. Comput. Acoust.*, vol. 26, no. 2, Jun. 2018, Art. no. 1850018.

[28] S. Marburg, "Numerical damping in the acoustic boundary element method," *Acta Acustica United Acustica*, vol. 102, no. 3, pp. 415–418, May 2016.

[29] A. Buffa and S. Sauter, "On the acoustic single layer potential: Stabilization and Fourier analysis," *SIAM J. Scientific Comput.*, vol. 28, no. 5, pp. 1974–1999, Jan. 2006.

[30] L. Banjai and S. Sauter, "A refined Galerkin error and stability analysis for highly indefinite variational problems," *SIAM J. Numer. Anal.*, vol. 45, no. 1, pp. 37–53, Jan. 2007.

[31] M. Löhndorf and J. M. Melenk, "Wavenumber-explicit *hp*-BEM for high frequency scattering," *SIAM J. Numer. Anal.*, vol. 49, no. 6, pp. 2340–2363, Jan. 2011.

[32] J. M. Melenk, "Mapping properties of combined field Helmholtz boundary integral operators," *SIAM J. Math. Anal.*, vol. 44, no. 4, pp. 2599–2636, Jan. 2012.

[33] M. Zworski, *Semiclassical Analysis*. Providence, RI, USA: American Mathematical Society, 2012.

[34] G. C. Hsiao and W. L. Wendland, *Boundary Integral Equations*. Berlin, Germany: Springer, 2008.

[35] J. Galkowski, M. Rachh, and E. A. Spence, "Helmholtz boundary integral methods and the pollution effect," 2026, *arXiv:2507.22797*.

[36] M. E. Masciocchi, E. Citraro, A. Dély, L. Rahmouni, A. Merlini, and F. P. Andriulli, "On some operator filtering strategies based on suitably modified Green's functions," in *Proc. Int. Conf. Electromagn. Adv. Appl. (ICEAA)*, Oct. 2023, pp. 624–626.

[37] V. Giunzioni, A. Merlini, and F. P. Andriulli, "On a high-frequency analysis of some relevant integral equations in electromagnetics," in *Proc. Int. Conf. Electromagn. Adv. Appl. (ICEAA)*, Portugal, Sep. 2024, pp. 821–824.

[38] M. Abramowitz and I. A. Stegun, *Handbook of Mathematical Functions: With Formulas, Graphs, and Mathematical Tables*, vol. 55. North Chelmsford, MA, USA: Courier Corporation, 1964.

[39] A. Peterson, S. Ray, and R. Mittra, *Computational Methods for Electromagnetics* (IEEE/OUP Series on Electromagnetic Wave Theory). New York, NY, USA: IEEE Press, 1998.

[40] J. D. Jackson, *Classical Electrodynamics*, 3rd ed., Hoboken, NJ, USA: Wiley, 1999.

[41] W. C. Chew, *Waves and Fields in Inhomogeneous Media*. New York, NY, USA: IEEE Press, 1995.

[42] S. B. Adrian, A. Dély, D. Consoli, A. Merlini, and F. P. Andriulli, "Electromagnetic integral equations: Insights in conditioning and preconditioning," *IEEE Open J. Antennas Propag.*, vol. 2, pp. 1143–1174, 2021.

[43] J. R. Mautz and R. F. Harrington, "H-field, E-field, and combined field solutions for conducting body of revolution," *Archiv Elektronik und Uebertragungstechnik*, vol. 32, pp. 157–164, Apr. 1978.

[44] K. E. Warnick and W. Cho Chew, "Accuracy of the method of moments for scattering by a cylinder," *IEEE Trans. Microw. Theory Techn.*, vol. 48, no. 10, pp. 1652–1660, Oct. 2000.

[45] M. Darbas, "Préconditionneurs analytiques de type Calderon pour les formulations Intégrales Des.Problèmes de diffraction d'ondes," Ph.D. dissertation, Institut National des Sciences Appliquées de Toulouse (INSA Toulouse), Toulouse, France, Nov. 2004.

[46] F. P. Andriulli, I. Bogaert, and K. Cools, "On the high frequency behavior and stabilization of a preconditioned and resonance-free formulation," in *Proc. Int. Conf. Electromagn. Adv. Appl. (ICEAA)*, Sep. 2015, pp. 1321–1324.

[47] D. Consoli et al., "On the fast direct solution of a preconditioned electromagnetic integral equation," in *Proc. Int. Conf. Electromagn. Adv. Appl. (ICEAA)*, South Africa, Sep. 2022, pp. 193–195.

[48] X. Antoine, M. Darbas, and Y. Y. Lu, "An improved surface radiation condition for high-frequency acoustic scattering problems," *Comput. Methods Appl. Mech. Eng.*, vol. 195, nos. 33–36, pp. 4060–4074, Jul. 2006.

[49] M. Darbas, "Generalized combined field integral equations for the iterative solution of the three-dimensional Maxwell equations," *Appl. Math. Lett.*, vol. 19, no. 8, pp. 834–839, Aug. 2006.

[50] Y. Boubendir and C. Turc, "Well-conditioned boundary integral equation formulations for the solution of high-frequency electromagnetic scattering problems," *Comput. Math. Appl.*, vol. 67, no. 10, pp. 1772–1805, Jun. 2014.

[51] G. C. Hsiao and R. E. Kleinman, "Error analysis in numerical solution of acoustic integral equations," *Int. J. Numer. Methods Eng.*, vol. 37, no. 17, pp. 2921–2933, Sep. 1994.

[52] R. J. Adams, "Physical and analytical properties of a stabilized electric field integral equation," *IEEE Trans. Antennas Propag.*, vol. 52, no. 2, pp. 362–372, Feb. 2004.

[53] V. Domínguez, I. G. Graham, and V. P. Smyshlyaev, "A hybrid numerical-asymptotic boundary integral method for high-frequency acoustic scattering," *Numerische Math.*, vol. 106, no. 3, pp. 471–510, May 2007.

[54] K. F. Warnick and W. C. Chew, "On the spectrum of the electric field integral equation and the convergence of the moment method," *Int. J. Numer. Methods Eng.*, vol. 51, no. 1, pp. 31–56, May 2001.

[55] C. P. Davis and K. F. Warnick, "Error analysis of 2-D MoM for MFIE/EFIE/CFIE based on the circular cylinder," *IEEE Trans. Antennas Propag.*, vol. 53, no. 1, pp. 321–331, Jan. 2005.

[56] K. F. Warnick and W. C. Chew, *Numerical Analysis for Electromagnetic Integral Equations*. Norwood, MA, USA: Artech House, 2008.

[57] M. Darbas and F. L. Louër, "Well-conditioned boundary integral formulations for high-frequency elastic scattering problems in three dimensions," *Math. Methods Appl. Sci.*, vol. 38, no. 9, pp. 1705–1733, Jun. 2015.

[58] F. W. J. Olver, *NIST Handbook of Mathematical Functions*. Cambridge, U.K.: Cambridge Univ. Press, 2010.

[59] S. N. Chandler-Wilde and D. P. Hewett, "Wavenumber-explicit continuity and coercivity estimates in acoustic scattering by planar screens," *Integral Equ. Operator Theory*, vol. 82, no. 3, pp. 423–449, Jul. 2015.

[60] C. P. Davis and K. F. Warnick, "On the physical interpretation of the sobolev norm in error estimation," *Appl. Comput. Electromagn. Soc. J. (ACES)*, vol. 20, no. 2, pp. 144–150, 2005.

[61] X. Antoine and M. Darbas, "Integral equations and iterative schemes for acoustic scattering problems," in *Numerical Methods for Acoustics Problems*, F. Magoulès, Ed., Saxe-Coburg Editors, 2016.

[62] S. Christiansen, "Discrete Fredholm properties and convergence estimates for the electric field integral equation," *Math. Comput.*, vol. 73, no. 245, pp. 143–167, Jul. 2003.

[63] F. Boeykens, H. Rogier, J. Van Hese, J. Sercu, and T. Boonen, "Rigorous analysis of internal resonances in 3-D hybrid FE-BIE formulations by means of the Poincaré–Steklov operator," *IEEE Trans. Microw. Theory Techn.*, vol. 61, no. 10, pp. 3503–3513, Oct. 2013.

[64] T. Betcke, J. Phillips, and E. A. Spence, "Spectral decompositions and nonnormality of boundary integral operators in acoustic scattering," *IMA J. Numer. Anal.*, vol. 34, no. 2, pp. 700–731, Apr. 2014.

[65] V. Giunzioni, A. Merlini, and F. P. Andriulli, "Spectral analysis of discretized boundary integral operators in 3D: A high-frequency perspective," in *Proc. Int. Conf. Electromagn. Adv. Appl. (ICEAA)*, Palermo, Italy, Sep. 2025, pp. 1316–1319.



Viviana Giunzioni (Member, IEEE) received the B.Sc. and M.Sc. degrees (cum laude) in electronic engineering and the Ph.D. degree (cum laude) in electrical, electronics, and communications engineering from the Politecnico di Torino, Turin, Italy, in 2019, 2021, and 2025, respectively.

She has been an Assistant Professor with the Department of Electronics and Telecommunications, Politecnico di Torino, since March 2026. She was a co-author of two AP-S/URSI honorable mention articles in 2026. Her research interests include computational electromagnetics, boundary integral formulations, preconditioning strategies, and fast iterative and direct solvers for integral equations, with applications to antennas, microwave structures, terahertz dosimetry, and biomedical imaging.

Dr. Giunzioni received the IEEE AP-S Doctoral Research Grant Award in 2022, the Honorable Mention at the IEEE AP-S/URSI Symposium in 2022, the Honorable Mention at the URSI General Assembly and Scientific Symposium in 2023, the IEEE Antennas and Propagation Society Fellowship in 2024, and the Young Scientist Award from the URSI International Symposium on Electromagnetic Theory in 2025. She was the finalist for the Young Scientist Award at ICEAA.



Adrien Merlini (Senior Member, IEEE) received the M.Sc. Eng. degree from the École Nationale Supérieure des Télécommunications de Bretagne (Télécom Bretagne), Brest, France, in 2015, and the Ph.D. degree from the École Nationale Supérieure Mines-Télécom Atlantique (IMT Atlantique), Brest, in 2019.

From 2018 to 2019, he was a Visiting Ph.D. Student with the Politecnico di Torino, Turin, Italy, where he became a Research Associate. Since 2019, he has been an Associate Professor with the Microwave Department, IMT Atlantique. He has authored award-winning articles, including a third-place finish at the EMTS 2023 Best Paper Competition, the 2022 ICEAA–IEEE APWC Best Paper Award, seven honorable mentions (URSI/IEEE–APS 2021, 2022, 2023, and 2026), and three best paper finalist recognitions (URSI GASS 2020 and URSI/IEEE–APS 2021 and 2022). His research interests include preconditioning and acceleration of integral equation solvers for electromagnetic simulations and their application to brain imaging.

Dr. Merlini received young scientist awards at URSI GASS 2020, EMTS 2023, and URSI AP-RASC 2025. He is a member of IEEE-HKN, the IEEE Antennas and Propagation Society, URSI France, and Lab-STICC. He serves as an Associate Editor and a Column Editor for *IEEE Antennas and Propagation Magazine*.



Francesco P. Andriulli (Fellow, IEEE) received the Laurea degree in electrical engineering from the Politecnico di Torino, Turin, Italy, in 2004, the M.Sc. degree in electrical engineering and computer science from the University of Illinois Chicago, Chicago, IL, USA, in 2004, and the Ph.D. degree in electrical engineering from the University of Michigan, Ann Arbor, MI, USA, in 2008.

From 2008 to 2010, he was a Research Associate with the Politecnico di Torino. He was an Associate Professor from 2010 to 2014 and then a Full Professor from 2014 to 2017 with the École Nationale Supérieure Mines-Télécom Atlantique (IMT Atlantique), Brest, France. Since 2017, he has been a Full Professor with the Politecnico di Torino. His research interests are in computational electromagnetics including frequency- and time-domain integral equation solvers, well-conditioned formulations, fast solvers, low-frequency electromagnetic analyses, and modeling techniques for antennas, wireless components, microwave circuits, and biomedical applications, with a special focus on brain imaging.

Prof. Andriulli received several best paper awards at conferences and symposia (International Union of Radio Science (URSI) NA 2007, IEEE AP-S 2008, and ICEAA IEEE-APWC 2015) and also in co-authorship with his students and collaborators (EMTS 2025, ICEAA IEEE-APWC 2021, EMTS 2016, URSI-DE Meeting 2014, and ICEAA 2009) with whom he received a second prize conference paper (URSI GASS 2014), a third prize conference paper (IEEE–APS 2018), seven honorable mention conference papers (ICEAA 2011, URSI/IEEE–APS 2013, four in URSI/IEEE–APS 2022, and URSI/IEEE–APS 2023), and other four finalist conference papers (URSI/IEEE–APS 2012, URSI/IEEE–APS 2007, URSI/IEEE–APS 2006, and URSI/IEEE–APS 2022). Moreover, he received the 2014 IEEE AP-S Donald G. Dudley Jr. Undergraduate Teaching Award, the Triennium 2014–2016 URSI Issac Koga Gold Medal, and the 2015 L. B. Felsen Award for Excellence in Electrodynamics. He is a fellow of URSI and a member of Eta Kappa Nu, Tau Beta Pi, and Phi Kappa Phi. He serves as the 2026 President-Elect of the IEEE Antennas and Propagation Society and served as the IEEE AP-S Vice President of Publications in 2025, the Editor-in-Chief for *IEEE Antennas and Propagation Magazine*, a Track Editor for IEEE TRANSACTIONS ON ANTENNAS AND PROPAGATION, and an Associate Editor for IEEE ANTENNAS AND WIRELESS PROPAGATION LETTERS, IEEE ACCESS, *URSI Radio Science Letters*, and *IET Microwaves, Antennas & Propagation* (MAP).

Open Access funding provided by Politecnico di Torino within the CRUI CARE Agreement